






# On the Properties of X-Ray Corona in Seyfert 1 Galaxies

Indrani Pal<sup>1,2,3</sup> , Anju A.<sup>4</sup>, H. Sreehari<sup>1,5</sup>, Gitika Rameshan<sup>6</sup>, C. S. Stalin<sup>1</sup>, Claudio Ricci<sup>7,8</sup> , and S. Marchesi<sup>3,9,10</sup> <sup>1</sup> Indian Institute of Astrophysics, Bangalore, 560034, Karnataka, India<sup>2</sup> Pondicherry University, R.V. Nagar, Kalapet, 605014, Puducherry, India<sup>3</sup> Department of Physics and Astronomy, Clemson University, Kinard Lab of Physics, Clemson, SC 29634, USA<sup>4</sup> Department of Physical Sciences, Indian Institute of Science Education And Research Kolkata, Mohanpur, Nadia-741246, West Bengal, India<sup>5</sup> Department of Physics, Faculty of Natural Sciences, University of Haifa, Mount Carmel, Haifa 3498838, Israel<sup>6</sup> Cochin University of Science and Technology, South Kalamassery, Kochi, Kerala, 682022, India<sup>7</sup> Instituto de Estudios Astrofísicos, Facultad de Ingeniería y Ciencias, Universidad Diego Portales, Avenida Ejército Libertador 441, Santiago, Chile<sup>8</sup> Kavli Institute for Astronomy and Astrophysics, Peking University, Beijing 100871, People's Republic of China<sup>9</sup> Dipartimento di Fisica e Astronomia (DIFA), Università di Bologna, via Gobetti 93/2, I-40129 Bologna, Italy<sup>10</sup> INAF—Osservatorio di Astrofisica e Scienza dello Spazio di Bologna, Via Piero Gobetti, 93/3, 40129, Bologna, Italy

Received 2023 October 26; revised 2024 September 20; accepted 2024 September 21; published 2024 November 19

## Abstract

We carried out a uniform and systematic analysis of a sample of 112 nearby bright Seyfert 1 type active galactic nuclei, the observations of which were carried out by the Nuclear Spectroscopic Telescope Array between 2013 August and 2022 May. The main goal of this analysis is to investigate the nature of the X-ray corona in Seyfert 1 galaxies. By fitting a physical model to the NuSTAR spectra, we could constrain the high-energy cutoff ( $E_{\text{cut}}$ ) for 73 sources in our sample. To estimate the temperature of the corona ( $kT_e$ ) in our sample of 112 sources, we used the Comptonization model to fit their spectra. We could constrain  $kT_e$  in 42 sources. We found a strong positive correlation between  $E_{\text{cut}}$  and  $kT_e$ , with most of the sources lying above the empirical approximation of  $E_{\text{cut}} = 2-3 kT_e$ . We investigated for possible correlations between various properties of the corona obtained from physical model fits to the observed spectra and between various coronal parameters and physical properties of the sources such as Eddington ratio and black hole mass. We found (a) a strong correlation between  $E_{\text{cut}}$  and the photon index and (b) a significant negative correlation between  $kT_e$  and the optical depth. From detailed statistical analysis of the correlation of coronal parameters with the Eddington ratio and black hole mass, we found no significant correlation. The correlations observed in this study indicate that an optically thin corona is needed to sustain a hotter corona with a steeper spectrum.

*Unified Astronomy Thesaurus concepts:* Seyfert galaxies (1447); Active galactic nuclei (16); X-ray active galactic nuclei (2035)

## 1. Introduction

Most massive galaxies host supermassive black holes (SMBHs) at their centers with masses ( $M_{\text{BH}}$ ) of the order of  $10^5-10^{10} M_{\odot}$ . These SMBHs power active galactic nuclei (AGN) by accretion of matter from their surroundings (E. E. Salpeter 1964; D. Lynden-Bell 1969; N. I. Shakura & R. A. Sunyaev 1973; P. W. Guilbert et al. 1983; L. C. Ho 2008). The observed optical, ultraviolet (UV) radiation from these accretion-powered systems is believed to be thermal emission from the standard optically thick, geometrically thin accretion disk (G. A. Shields 1978; M. A. Malkan & W. L. W. Sargent 1982; W.-H. Sun & M. A. Malkan 1989) that surrounds the SMBHs. These AGN are also sources of intense X-ray emission (M. Elvis et al. 1978; R. F. Mushotzky et al. 1993). The X-ray emission in the radio-quiet category of AGN is believed to originate from a compact region that contains hot electrons ( $T_e \sim 10^{8-9}$  K) called the corona situated close to the vicinity of the SMBH. Observations indicate that the corona is physically compact with size scales of the order of  $3-10 R_G$  (I. M. McHardy et al. 2005; G. Risaliti et al. 2005), where  $R_G$  is the gravitational radius defined as  $R_G = GM_{\text{BH}}/c^2$ ; here,  $G$  is the gravitational constant and  $c$  is the speed of light. The hot electrons in the corona, inverse Compton scatter the optical or UV thermal

photons from the geometrically thin, optically thick accretion disk, thereby producing X-ray emission (F. Haardt & L. Maraschi 1991, 1993). The emergent X-ray spectrum follows a power law with the high-energy roll-off of the form  $N(E) \propto E^{-\Gamma} \exp(-E/E_{\text{cut}})$ , where  $\Gamma$  is the power-law photon index and  $E_{\text{cut}}$  is the high-energy cutoff (R. A. Sunyaev & L. G. Titarchuk 1980). In this paradigm, expecting a connection between the accretion disk and the X-ray-emitting corona is natural. One piece of observational evidence for this accretion disk–corona connection is the observed positive correlation (O. Shemmer et al. 2008; G. Risaliti et al. 2009; C. Jin et al. 2012; H. Liu et al. 2021; A. Tortosa et al. 2023) between  $\Gamma$  and the mass-normalized accretion rate usually represented by the Eddington ratio ( $\lambda_{\text{Edd}} = L_{\text{bol}}/L_{\text{Edd}}$ ). Here,  $L_{\text{bol}}$  is the bolometric luminosity and  $L_{\text{Edd}}$  is the Eddington luminosity defined as  $L_{\text{Edd}} = 1.3 \times 10^{38} M_{\text{BH}}/M_{\odot} \text{ erg s}^{-1}$ . A possible explanation for this observed correlation is that at a higher  $\lambda_{\text{Edd}}$ , the increased optical/UV photons from the accretion disk can lead to a more effective cooling of the corona, thereby leading to a decrease in the temperature of the corona ( $kT_e$ ) and larger  $\Gamma$  or softening of the X-ray spectrum. Recently, C. Ricci et al. (2018) proposed that another explanation for this is the pair thermostat, due to the changes in temperature across the compactness–temperature ( $l - \theta$ ) plane, and they could successfully reproduce the slope of the  $\Gamma - \lambda_{\text{Edd}}$  correlation.

According to Comptonization models, for a corona with slab geometry,  $E_{\text{cut}}$  is related to the temperature of the corona as  $E_{\text{cut}} = 2-3 kT_e$  for optically thin and thick plasma, respectively

(P. O. Petrucci et al. 2001). However, according to T. Liu et al. (2014), the relation between  $E_{\text{cut}}$  and  $kT_e$  cannot be simple in the case of the nonstatic corona. Also, R. Middei et al. (2019) have shown that the relation of  $E_{\text{cut}} = 2-3 kT_e$  is only valid for low values of  $kT_e$  and  $\tau$ . Recently, for the source MR 2251-178, I. Pal et al. (2022) found  $E_{\text{cut}} = 4.84 \pm 0.11 kT_e$ , which deviates from the generally considered relation between  $E_{\text{cut}}$  and  $kT_e$  (P. O. Petrucci et al. 2001). Also,  $\Gamma$  is expected to depend on various parameters of the corona, such as its temperature  $kT_e$ , the optical depth ( $\tau$ ) as well as the seed photon temperature. To understand the properties of AGN, it is important to have better constraints on the coronal parameters of AGN that characterize the X-ray emission, such as  $\Gamma$  and  $kT_e$ .

Earlier studies on the determination of the temperature of the corona in Seyfert galaxies used data from high-energy instruments such as CGRO (W. N. Johnson et al. 1997; A. A. Zdziarski et al. 2000), BeppoSAX (F. Nicastro et al. 2000; M. Dadina 2007), INTEGRAL (P. Lubiński et al. 2010, 2016; A. Malizia et al. 2014), Swift-Burst Alert Telescope (BAT; R. V. Vasudevan et al. 2013; C. Ricci et al. 2017, 2018), and Suzaku (F. Tazaki et al. 2011). These studies have found that in Seyfert galaxies, the coronal temperature shows a wide range, with the values of  $E_{\text{cut}}$  ranging from 50 to 500 keV. These less sensitive observations were, however, limited to nearby bright Seyfert galaxies. Increased interest in studies on the hard X-ray spectra of AGN, as well as the determination of its coronal temperature, happened after the launch of the Nuclear Spectroscopic Telescope Array (NuSTAR; F. A. Harrison et al. 2013) in 2012, due to its wide spectral coverage of 3–79 keV and its high sensitivity beyond 10 keV. Since its launch, values of the temperature of the corona have become known for many AGN, but most of those studies are restricted to the determination of  $E_{\text{cut}}$ . Also, data from NuSTAR have led to the finding of the variation in  $kT_e$  (S. Barua et al. 2020, 2021; J.-L. Kang et al. 2021; I. Pal et al. 2022; I. Pal & C. S. Stalin 2023) as well as  $E_{\text{cut}}$  (D. R. Ballantyne et al. 2014; F. Ursini et al. 2015, 2016; L. Keek & D. R. Ballantyne 2016; A. Zoghbi et al. 2017; J.-X. Zhang et al. 2018; J.-L. Kang et al. 2021).

In recent years, there have been several studies on characterizing the temperature of the corona ( $E_{\text{cut}}$  or  $kT_e$ ) in samples of AGN (N. Kamraj et al. 2018; A. Tortosa et al. 2018; M. Molina et al. 2019; P. Rani et al. 2019; M. Baloković et al. 2020; J. Kang et al. 2020; C. Panagiotou & R. Walter 2020; A. Akylas & I. Georgantopoulos 2021; J. T. Hinkle & R. Mushotzky 2021; N. Kamraj et al. 2022; J.-L. Kang & J.-X. Wang 2022; I. Pal & C. S. Stalin 2023). Most of these studies focused on the determination of  $E_{\text{cut}}$  from phenomenological model fits to the observed X-ray spectra. Though  $E_{\text{cut}}$  can serve as a good proxy for  $kT_e$ , the recent findings of deviation from the  $E_{\text{cut}} = 2-3 kT_e$  in a few sources have necessitated the determination of  $kT_e$  in AGN based on a physical model fit to the observed X-ray spectra. The literature also contains results on  $E_{\text{cut}}/kT_e$  values and their correlation with other physical parameters. However, these correlations vary between studies, possibly due to small sample sizes and large error bars in the  $E_{\text{cut}}/kT_e$  measurements. Therefore, it is crucial to increase the sample size, analyze data consistently, and explore various correlations. To address these, we carefully selected type 1 sources with good signal-to-noise spectra from the NuSTAR archive and homogeneously conducted the needed analysis with a larger sample size than before.

In this work, we carried out an analysis of 112 Seyfert 1 type AGN to determine  $E_{\text{cut}}$  based on physical model fits to the NuSTAR data. Of these 112 sources, we could constrain  $E_{\text{cut}}$  in 73 sources. Further, physical model fits were carried out on the 112 sources to constrain  $kT_e$ . We could constrain  $kT_e$  in 42 sources. We investigated the correlation between different physical parameters obtained from the physical model fits. The selection of our sample of sources and data reduction are given in Section 2. We describe in Section 3 the model fits carried out on the data; the results are given in Sections 4 and 5, and a comparison of our findings on  $E_{\text{cut}}$  and  $kT_e$  with those found from the literature are given in Section 6, followed by a discussion and a summary in the final two sections. In this work, we adopted the cosmological parameters of  $H_0 = 70 \text{ km s}^{-1} \text{ Mpc}^{-1}$ ,  $\Omega_M = 0.3$ , and  $\Omega_\Lambda = 0.7$ . All the quoted uncertainties in the derived parameters were calculated at the 90% confidence level.

## 2. Sample Selection and Data Reduction

### 2.1. Sample Selection

Our sample of sources for this study was selected from the NuSTAR Master Catalog.<sup>11</sup> We examined publicly accessible data for Seyfert galaxies sourced either from the Swift-BAT 105 month catalog (K. Oh et al. 2018) or from the NASA/IPAC Extragalactic Database during the period spanning 2013 August to 2022 May. We found a total of 850 Seyfert galaxies. We selected only Seyfert 1 galaxies with a net count rate greater than  $0.1 \text{ counts s}^{-1}$  in the 3–79 keV band to have sufficiently good signal-to-noise ratio (S/N) spectrum for model fitting. Adopting the abovementioned criteria, we arrived at a final sample of 130 Seyfert 1 galaxies spanning the redshift interval of  $0.002 < z < 0.692$ . Of these 130 sources, around 90% of the sources were studied in C. Ricci et al. (2017). C. Ricci et al. (2017) carried out a broadband (0.3–150 keV) X-ray spectroscopic analysis of Swift-BAT selected sources by combining XMM-Newton, Swift/X-Ray Telescope (XRT), ASCA, Chandra, and Suzaku observations in the soft X-ray band with 70 months averaged Swift/BAT data. Based on the value of the line-of-sight column densities ( $N_{\text{H}}$ ) required in the absorption power-law fit, 18 sources were classified as obscured AGN ( $10^{22} \leq (N_{\text{H}} \text{ cm}^{-2}) < 10^{24}$ ) in C. Ricci et al. (2017). For this study, we selected the 112 unobscured nearby AGN with a median redshift of 0.035. We show in Figure 1 the redshift distribution for our sample of sources. The redshifts are taken from SIMBAD.<sup>12</sup> The full list of the Seyfert 1 galaxies and their NuSTAR observational details are given in Table 2. Among 112, about 50% of sources were observed more than once by NuSTAR. The observations with the highest exposure were chosen for this study to ensure good S/N spectra.

### 2.2. Data Reduction

For the 112 sources, we carried out the reduction of the raw event data taken from the HEASARC archive,<sup>13</sup> using the standard NuSTAR data reduction software NuSTARDAS<sup>14</sup> v1.9.3 distributed by HEASARC within HEASoft v6.26.1. We generated the calibrated and cleaned event files using the nupipeline task and the instrument responses taken from

<sup>11</sup> <https://heasarc.gsfc.nasa.gov/W3Browse/nustar/numaster.html>

<sup>12</sup> <http://simbad.cds.unistra.fr/simbad/>

<sup>13</sup> <https://heasarc.gsfc.nasa.gov/db-perl/W3Browse/w3browse.pl>

<sup>14</sup> [https://heasarc.gsfc.nasa.gov/docs/nustar/analysis/nustar\\_swguide.pdf](https://heasarc.gsfc.nasa.gov/docs/nustar/analysis/nustar_swguide.pdf)

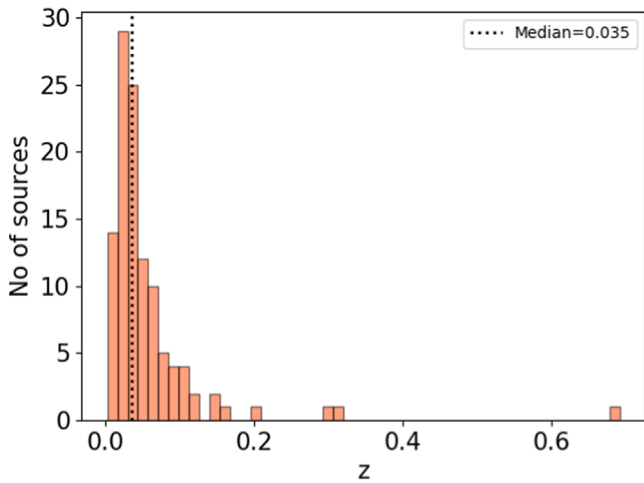


**Figure 1.** The redshift distribution of the sources. The vertical dotted line is the median of the distribution ( $z = 0.035$ ).

the NuSTAR calibration database (CALDB release 20190607). To exclude the periods of elevated background, we selected the filtering options SAACALC = 2, SAAMODE = OPTIMIZED, and TENTACLE = YES to consider the passage of the satellite through the South Atlantic Anomaly (SAA). The source regions for the 112 Seyferts were extracted using circular radii between  $30''$  and  $70''$  to maximize the S/N, depending on the source. A source-free circular area of the same radius on the same chip was selected to extract the background counts. All the science products, including energy spectra, response matrix files, and auxiliary response files, were generated using the task `nuproducts` for both the focal plane modules FPMA and FPMB. For spectral analysis, we fitted the background-subtracted spectra from FPMA and FPMB simultaneously using XSPEC version 12.10.1 (K. A. Arnaud 1996), allowing the cross-normalization factor to vary freely during spectral fits. The spectra were binned to have minimum counts of 20 per spectral energy bin. We note that, for faint sources, the binning of 20 counts  $\text{bin}^{-1}$  could be insufficient at the high-energy end with  $E > 50$  keV for the  $\chi^2$  statistics to be applicable. Also, it is likely that the choice of binning can have some effect on the derived  $E_{\text{cut}}$  or  $kT_e$  values. To verify this, we identified the 10 faintest sources in our sample and redid the analysis using a binning of 50 counts  $\text{bin}^{-1}$ . For those faint sources, we found that the  $E_{\text{cut}}$  values obtained using a binning of 50 counts  $\text{bin}^{-1}$  agree within errors to those obtained with a binning of 20 counts  $\text{bin}^{-1}$ . Therefore, it is likely that the binning choice adopted in this work has a negligible effect on the derived values of  $E_{\text{cut}}$  and/or  $kT_e$ . To get an estimate of the model parameters that best describe the observed data, we used the  $\chi^2$  statistics, and for calculating the errors in the model parameters, we used the  $\chi^2 = 2.71$  criterion, which is equivalent to the 90% confidence range in XSPEC.

### 3. Spectral Analysis

We carried out a detailed spectral analysis of the NuSTAR data in the energy range of 3–79 keV for the 112 sources, a few of which also have soft X-ray observations. Since these are unobscured Seyfert 1 galaxies, we do not have degeneracies between  $N_{\text{H}}$  and continuum parameters that have been found in obscured Seyfert 2 galaxies (S. Marchesi et al. 2018). Therefore, we chose to fit the NuSTAR data alone, and we

do not expect our results to be significantly affected by the lack of information at energies  $< 3$  keV. In the past, too, a similar approach has been followed in several studies (N. Kamraj et al. 2018; A. Tortosa et al. 2018; M. Baloković et al. 2020; S. H. Ezhikode et al. 2020; J. Kang et al. 2020; A. Akylas & I. Georgantopoulos 2021) aimed at characterizing the corona. For the completeness of our study, we compared our findings with those found in the literature where  $E_{\text{cut}}/kT_e$  were obtained with and without the soft X-ray coverage (see Table 3).

We used the following two models:

1. *Model 1.* CONST  $\times$  TBABS  $\times$  ZTBABS  $\times$  (XILLVER/RELXILL/(RELXILL+XILLVER)).
2. *Model 2.* CONST  $\times$  TBABS  $\times$  ZTBABS  $\times$  (XILLVERCP/RELXILLCP/(RELXILLCP+XILLVERCP)).

In both models, the Fe–K $\alpha$  line present in the source spectrum would be self-consistently taken care of. From our previous study (I. Pal et al. 2022; I. Pal & C. S. Stalin 2023), we confirmed that the model parameters, such as  $E_{\text{cut}}/kT_e/R$ , obtained using these models did not differ significantly from the best-fit measurements found from fitting the spectra with a phenomenological power law with a cutoff in which the Fe–K $\alpha$  line is not coupled with the reflection continuum.

In both our Model 1 and Model 2, CONST represents the calibration constant between the NuSTAR focal plane modules, FPMA and FPMB. TBABS was used to model the Milky Way Galactic hydrogen column density, which was taken from R. Willingale et al. (2013) for each source. The component ZTBABS represents the hydrogen column density ( $N_{\text{H}}^{\text{INT}}$ ) of the host galaxy. During the modeling of the source spectrum, the value of  $N_{\text{H}}^{\text{INT}}$  was allowed to vary freely.

XILLVER/RELXILL (J. García & T. R. Kallman 2010; J. García et al. 2011) was used to model the spectra with an absorbed cutoff power law along with the reflection features present in it. In XSPEC, Model 1 took the following forms:

1. *Model 1a.* CONST  $\times$  TBABS  $\times$  ZTBABS  $\times$  (XILLVER).
2. *Model 1b.* CONST  $\times$  TBABS  $\times$  ZTBABS  $\times$  (RELXILL).
3. *Model 1c.* CONST  $\times$  TBABS  $\times$  ZTBABS  $\times$  (RELXILL+XILLVER).

During the fit using Model 1a, the parameters that were kept free were  $\Gamma$ ,  $E_{\text{cut}}$ ,  $R$ , and the normalization ( $N_{\text{xillver}}$ ) of the XILLVER component. The reflector was considered neutral; therefore, we fixed the ionization parameter ( $\log \xi$ ) to 0.0. The values of  $AF_e$  and the inclination angle were fixed to the solar value ( $= 1.0$ ) and  $30^\circ$ , respectively.

In Model 1b, we replaced XILLVER with RELXILL to take care of the relativistic smeared Comptonization spectrum for a few sources. In addition to the parameters described in Model 1a, there are a few more parameters, such as the inner and outer emissivity indices ( $\beta_1$  and  $\beta_2$ , respectively), inner and outer radii of the accretion disk ( $r_{\text{in}}$  and  $r_{\text{out}}$ , respectively), break radius ( $r_{\text{br}}$ ) between  $r_{\text{in}}$  and  $r_{\text{out}}$ , and the spin of the black hole ( $a_*$ ). We tied  $\beta_1$  and  $\beta_2$  together during the fit and kept them as free parameters.  $r_{\text{br}}$ ,  $r_{\text{in}}$ , and  $r_{\text{out}}$  were fixed at their default values of  $15r_g$ ,  $3r_g$ , and  $400r_g$ , respectively. We considered a highly spinning SMBH and fixed  $a_*$  to 0.998 (K. S. Thorne 1974).  $AF_e$  was fixed to the solar value. The inclination angle was fixed to  $30^\circ$ . The other parameters that were kept free during the fit were  $\Gamma$ ,  $E_{\text{cut}}$ ,  $R$ ,  $\log \xi$ , and the normalization ( $N_{\text{relxill}}$ ) of the RELXILL model.

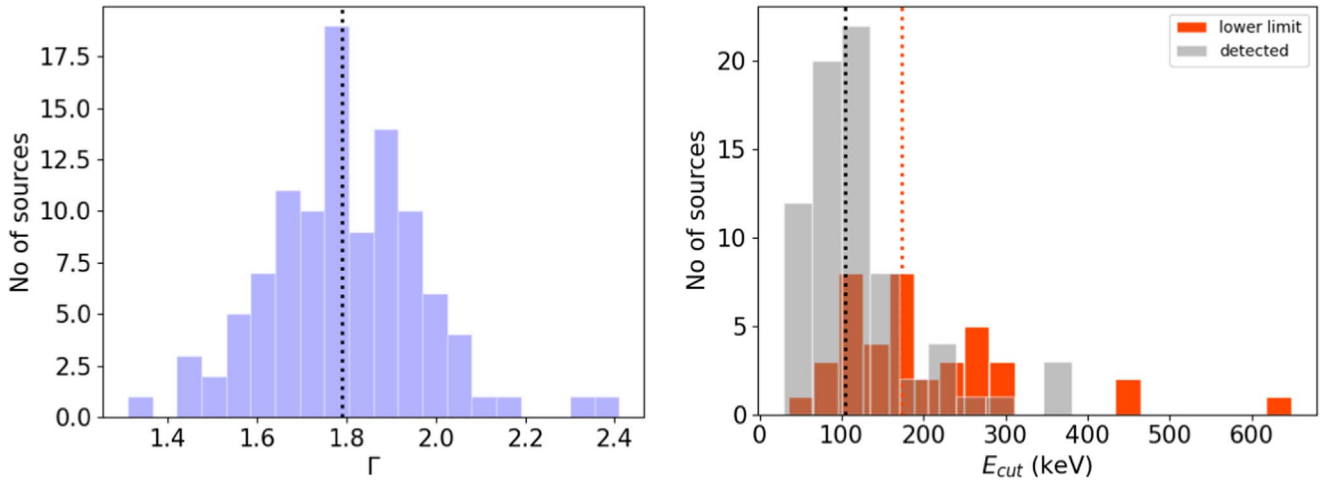


**Figure 2.** Distribution of  $\Gamma$  (left panel) and distribution of  $E_{\text{cut}}$  (right panel) obtained from Model 1 fit to all 112 source spectra. The vertical dotted lines are the median of the distributions.

The spectra of a few sources could not be well fitted using either XILLVER or RELXILL. In those sources where significant narrow Fe–K $\alpha$  emission lines were detected, we used Model 1c, in which we fitted RELXILL and XILLVER together. Between these two components  $\Gamma$ ,  $kT_e$ , and  $AF_e$  were tied together and kept as free parameters during the fitting. The other parameters were treated similarly as described earlier in Model 1a and Model 1b. We could constrain  $E_{\text{cut}}$  for 73 sources from the model fits. The summary of the spectral analysis from this model fits to the spectra given in Table 3.

Out of 112 sources, we used Model 1a in 86 sources to estimate different coronal parameters. In 20 out of the remaining 26 Seyferts, the presence of a broad emission line was confirmed. To take care of the relativistic broadening of the Fe–K $\alpha$  line, we fitted the spectra of those sources with Model 1b. In the other six sources (ARK 564, MCG-06-30-15, Mrk 1044, Mrk 279, NGC 3783, and NGC 4051), we used an XILLVER component in addition to RELXILL (Model 1c) since one model alone could not fit the reflection spectra properly. The distributions of  $\Gamma$  and  $E_{\text{cut}}$ , as found from the Model 1 fits, are given in Figure 2. The median value of  $\Gamma$ , as obtained from the analysis using Model 1, was found to be  $1.79 \pm 0.02$ , which is consistent with the median value of  $\Gamma$  as found from the broadband analysis of the unobscured sources by C. Ricci et al. (2017). Using only the constrained  $E_{\text{cut}}$ , a median of  $104 \pm 8$  keV was obtained. The errors on the median values represent the statistical uncertainties, calculated as the standard deviation of the distribution divided by the square root of the sample size ( $\sigma/\sqrt{N}$ , where  $N$  is the number of data points). The broadband spectral fit using Model 1c with the data to model residue for the source Mrk 279 is presented in Figure 3.

We carried out the Comptonization model fits (Model 2) to the 112 sources to estimate the coronal temperature. We could constrain  $kT_e$  for 42 sources using this model. In XSPEC, Model 2 took the following forms:

1. *Model 2a.* CONST  $\times$  TBABS  $\times$  ZTBABS  $\times$  (XILLVERCP).
2. *Model 2b.* CONST  $\times$  TBABS  $\times$  ZTBABS  $\times$  (RELXILLCP).
3. *Model 2c.* CONST  $\times$  TBABS  $\times$  ZTBABS  $\times$  (RELXILLCP +XILLVERCP).

All the model parameters were handled similarly as described for Model 1. The best-fit values of various coronal

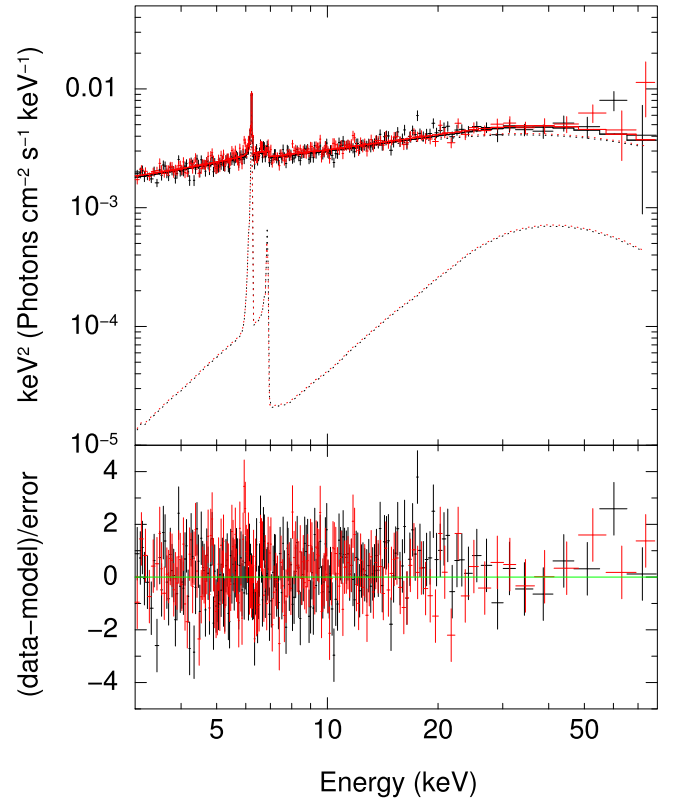


**Figure 3.** The best-fit unfolded FPMA/FPMB spectra of Mrk 279 (upper panel) with data to model residue of the Model 1c fit to the source spectra (lower panel).

parameters found from the Comptonization model fit (Model 2) are given in Table 4. The distribution of the best-fit values of  $\Gamma$  and  $kT_e$ , as obtained from Model 2, are shown in Figure 4. The median value of  $\Gamma$  was determined to be  $1.86 \pm 0.01$ , and when considering only the constrained value of  $kT_e$ , the median was found to be  $24 \pm 2$  keV.

#### 4. Relation between $E_{\text{cut}}$ and $kT_e$

It is believed that the phenomenological high-energy cutoff could be related to the temperature as  $E_{\text{cut}} = 2\text{--}3 kT_e$

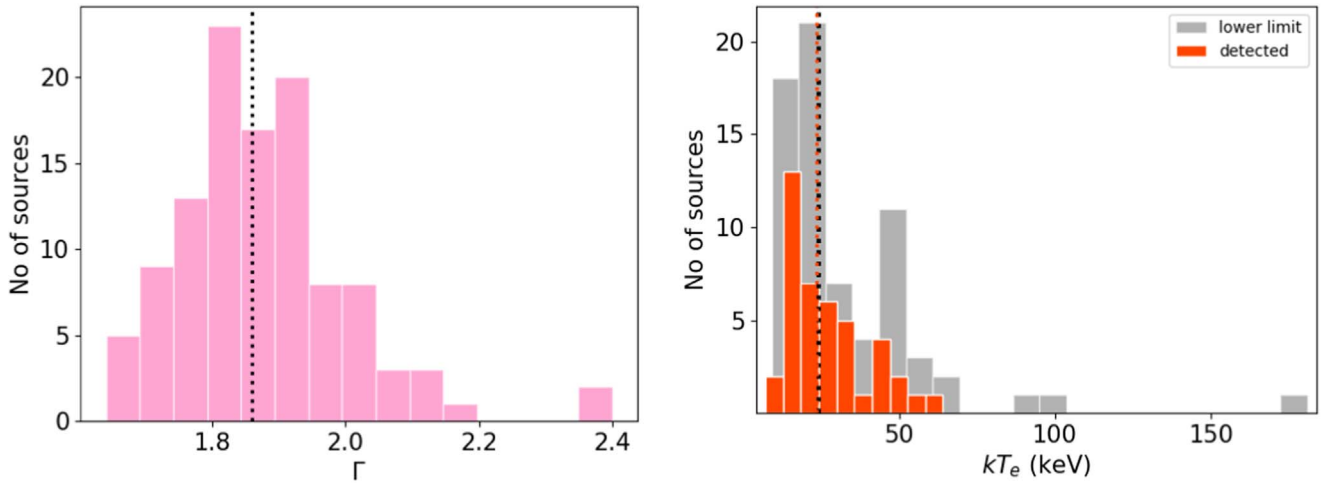


**Figure 4.** Distribution of  $\Gamma$  (left panel) and  $kT_e$  (right panel) from Model 2 fit for 112 sources. The vertical dotted lines are the median of the distributions.

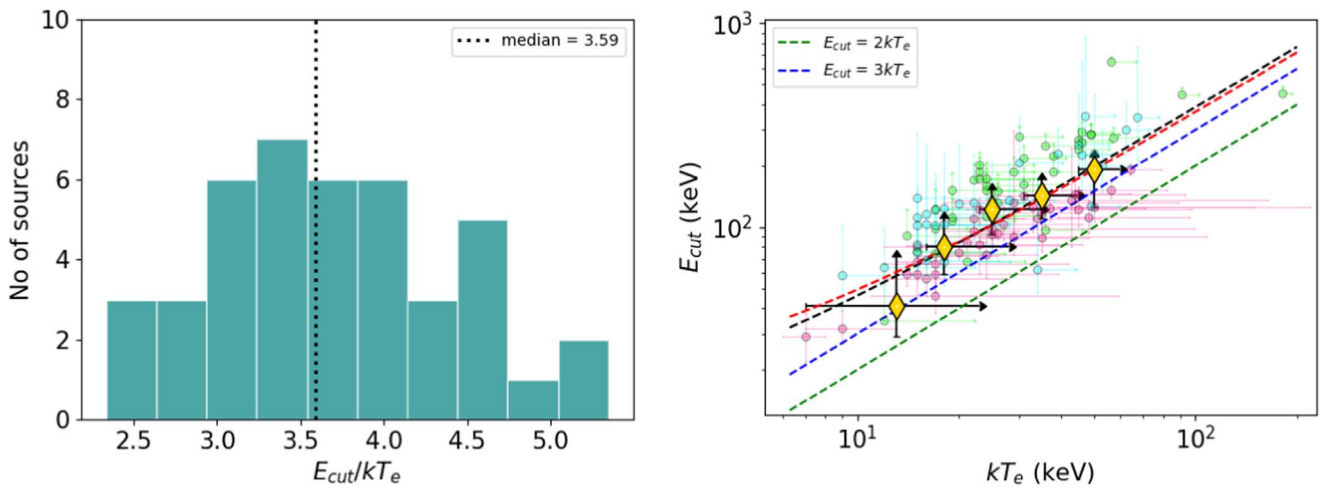


**Figure 5.** Distribution of the ratio between  $E_{\text{cut}}$  to  $kT_e$  for the 42 sources with  $kT_e$  measurements (left panel). The vertical dotted line is the median of the ratio. The variation of  $E_{\text{cut}}$  against  $kT_e$  (right panel). Here, the green dashed line shows the  $E_{\text{cut}} = 2kT_e$  relation, and the blue dashed line shows the  $E_{\text{cut}} = 3kT_e$  relation. The black dashed line is the linear least squares fit to the median values of  $E_{\text{cut}}$  (yellow diamond points) obtained from the KMPL survival analysis in each  $kT_e$  bin. The best fit is  $E_{\text{cut}} = (3.80 \pm 0.53)kT_e + (8.15 \pm 16.51)$ . The red dashed line is the linear relation obtained from the statistical analysis package ASURV. The pink dots with error bars are the constrained values, and the green dots represent the censored values of  $E_{\text{cut}}$  and  $kT_e$ ; the cyan dots denote the constrained values of  $E_{\text{cut}}$  and lower limits of  $kT_e$ .

(P. O. Petrucci et al. 2001). However, recent studies do indicate that this simple relation between  $E_{\text{cut}}$  and  $kT_e$  may not be valid for all sources (T. Liu et al. 2014; R. Middei et al. 2019; I. Pal et al. 2022). The relation can be complicated in the case of a nonstatic corona, such as the one with outflows (T. Liu et al. 2014). Also, according to R. Middei et al. (2019), the relation of  $E_{\text{cut}} = 2-3kT_e$  is valid only for low values of  $\tau$  and  $kT_e$ . The authors also argued that if the origin of the X-ray emission is different than the thermal Comptonization, the typical relation between  $E_{\text{cut}}$  and  $kT_e$  may not hold. We show in the left panel of Figure 5 the distribution of the ratio between  $E_{\text{cut}}$  to  $kT_e$  for 42 sources for which we could constrain both  $E_{\text{cut}}$  and  $kT_e$ . We found the ratio to vary between 2.33 and 5.35, with a median of 3.59 in 42 sources. In the right panel of Figure 5 is shown the distribution of the sources in the  $E_{\text{cut}}$  versus  $kT_e$  plane. We excluded the sources with  $E_{\text{cut}} > 300$  keV from this correlation analysis since at the high-energy limit, the best-fit  $kT_e$  values obtained using the Comptonization model produce comparatively lower corona temperature than that obtained using a cutoff power law (A. A. Zdziarski et al. 2003; A. C. Fabian et al. 2015).

To include the lower limits of  $E_{\text{cut}}$  and  $kT_e$  in our calculation, we performed a survival analysis method using the nonparametric Kaplan–Meier product limit (KMPL) approach in Python.<sup>15</sup> The yellow points in the plot represent the median values of  $E_{\text{cut}}$  in different  $kT_e$  bins obtained from the survival analysis method using the KMPL approach. The errors in the median values of  $E_{\text{cut}}$  and  $kT_e$  were estimated with 95% confidence. Also, shown in the same figure are the  $E_{\text{cut}} = 2kT_e$  (red dashed) and  $E_{\text{cut}} = 3kT_e$  (blue dashed) lines. From the linear least squares fit to the estimated median values of  $E_{\text{cut}}$  in different  $kT_e$  bins (black dashed line in Figure 5), we found

$$E_{\text{cut}} = (3.80 \pm 0.53)kT_e + (8.15 \pm 16.51). \quad (1)$$

We calculated the Pearson’s correlation coefficient and the null hypothesis probability for no correlation to check the significance of the linear fit, and we found  $r = 0.97$  and  $p = 0.006$ . We also used the Astronomy SURVival Analysis

<sup>15</sup> <https://medium.com/the-researchers-guide/survival-analysis-in-python-km-estimate-cox-ph-and-aft-model-5533843c5d5d>

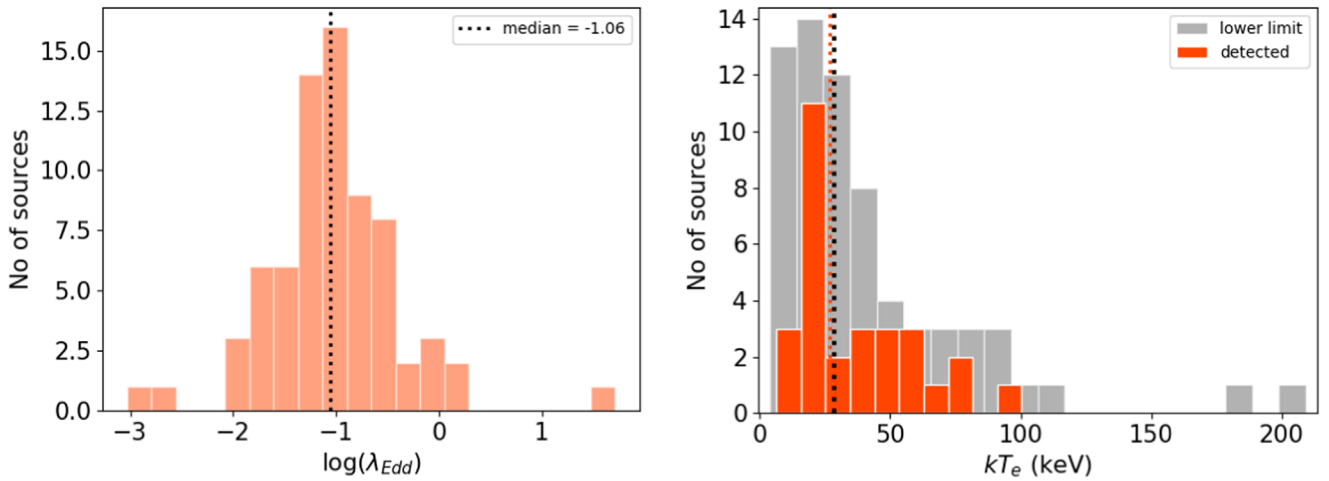


**Figure 6.** Left panel: Eddington ratio distribution for the 109 sources for which we could find the black hole mass from the literature. Right panel: distribution of both constrained and censored values of  $kT_e$  as calculated using Equation (1) from the  $E_{\text{cut}}$  values taken from C. Ricci et al. (2018) for 96 sources in common between this work and that of C. Ricci et al. (2018). The vertical dotted lines are the median of the distributions.

(ASURV) package (E. D. Feigelson & P. I. Nelson 1985) to take into account the lower limits in the  $E_{\text{cut}}$  and  $kT_e$  measurements. We derived the bivariate correlation and linear regression parameters using Spearman’s rank correlation coefficient ( $\rho$ ) and the Schmitt method and found  $E_{\text{cut}} = 3.54 kT_e + 13.99$ . These observations thus indicate that for the sample of sources studied in this work,  $E_{\text{cut}}$  and  $kT_e$  maintain a strong correlation with most of our sources lying above the  $E_{\text{cut}} = 3 kT_e$  line.

### 5. Correlation Analysis

This section presents the correlation analysis between different best-fitted model parameters obtained using Model 1. We also discussed the correlation between the coronal properties and the physical properties of the sources, such as  $\lambda_{\text{Edd}}$  and  $M_{\text{BH}}$ . For the latter, we had to exclude three sources from the correlation analysis, namely, ESO 416–G002, IRAS F12397+3333, and UGC 10120, as we did not find a black hole mass ( $M_{\text{BH}}$ ) measurement for them in the literature. We adopted black hole mass estimates from the second data release of optical broad emission line measurements from the BASS survey (J. E. Mejía-Restrepo et al. 2022) except for ARK 564. The black hole mass for this source was taken from K. D. Denney et al. (2009).

For getting  $L_{\text{bol}}$ , we used the 2–10 keV intrinsic luminosity. The absorption and  $k$ -corrected intrinsic luminosities were converted to bolometric luminosities using the relation  $\log(L_{\text{bol}}) = 20 \times \log(L_{2-10 \text{ keV}})$  (R. V. Vasudevan & A. C. Fabian 2007). The distribution of the logarithm of the Eddington ratio ( $L_{\text{bol}}/L_{\text{Edd}} = \lambda_{\text{Edd}}$ ) for 109 sources is given in Figure 6.

The analysis of 112 sources using Model 1 revealed that  $E_{\text{cut}}$  could be constrained in 73 sources, while in the remaining 39 sources, only lower limits could be determined. These controlled  $E_{\text{cut}}$  measurements in 73 sources exhibited asymmetric errors, and  $E_{\text{cut}}$  in the remaining 39 sources only provided lower limits. From the measurements of  $kT_e$  also, we found constrained values in 42 sources, and the remaining 70 sources produced lower limits. In a few cases, we only found the upper limits of  $R$ . To account for the lower and upper limits in our correlation analysis, we used the KMPL approach, as described in Section 4. The median values of Parameter 2 (the dependent variable) were calculated using the KMPL method

for each bin of Parameter 1 (the independent variable), in cases where only the dependent variable had upper or lower limits. When both the dependent and independent variables had upper and lower limits, the KMPL estimator calculated the survival function based on the data status of the independent variable (censored = 0, constrained = 1) and determined the median value for each bin. For the dependent variable, the probability function and median value were calculated for the corresponding bins of independent variables using the KMPL estimator. To tackle the unconstrained values of the independent and dependent variables in the correlation analysis, we used the survival statistics within the ASURV FORTRAN package as well to calculate Spearman’s rank correlation coefficient ( $\rho$ ) and the probability of no correlation. We derived the linear regression intercepts and slopes using the Schmitt method in ASURV.

Though the survival analysis is well-suited to take care of the limits in the correlation analysis, it does not consider the asymmetric errors in the analysis. Thus, it is essential to consider both the asymmetric errors and lower limits in the correlation analysis. Therefore, we employed an approach similar to that described in I. Pal et al. (2022) to perform various correlation analyses and find the median of the parameters. The results of this analysis are given in Table 1.

We neglected the asymmetric errors associated with the controlled  $E_{\text{cut}}$  measurements in the initial approach and the lower limits. Instead, we solely considered the controlled best-fit values of  $E_{\text{cut}}$  and calculated the median values. We also performed correlation analysis using only those best-fit values between  $E_{\text{cut}}$  and other parameters by employing a logarithmic scale for fitting the parameters with a linear relation:

$$\log(y) = a \log(x) + b. \quad (2)$$

In the second approach, we included both controlled and limited values in the correlation analysis by incorporating the survival analysis using the KMPL test and found the median values of the dependent parameters in each bin of the independent variable. We also used the ASURV package to handle both constrained and unconstrained values of the parameters in the correlation analysis. To assess the strength of the linear correlation in both cases (Method IIa and IIb in Table 1), we computed Spearman’s

**Table 1**  
Results of the Correlation Analysis between Different Parameters

Parameter 1	Parameter 2	Method	Full Sample		Moderately Accreting Sources		Highly Accreting Sources	
			$\rho$	$p$	$\rho$	$p$	$\rho$	$p$
					$(\lambda_{\text{Edd}} < 0.1)$		$(\lambda_{\text{Edd}} > 0.1)$	
$E_{\text{cut}}$	$\lambda_{\text{Edd}}$	I	0.19	0.12	0.41	0.009	-0.02	0.89
		IIa	0.54	0.22	...	...	...	...
		IIb	0.06	0.55	0.11	0.39	-0.16	0.30
		III	0.03	0.75	0.12	0.37	-0.08	0.59
$R$	$\lambda_{\text{Edd}}$	IV	0.03	0.73	0.09	0.48	-0.08	0.61
		I	-0.28	0.01	-0.30	0.04	-0.07	0.68
		IIa	-0.25	0.05	...	...	...	...
		IIb	-0.22	0.02	-0.25	-0.06	-0.02	-0.88
$R$	$\Gamma$	III	-0.18	0.07	-0.21	0.11	-0.002	0.73
		I	0.28	0.009	...	...	...	...
		IIa	-0.55	0.26	...	...	...	...
$E_{\text{cut}}$	$R$	IIb	0.59	0.03	...	...	...	...
		III	0.30	0.002	...	...	...	...
		$E_{\text{cut}}$	-0.03	0.84	...	...	...	...
		IIa	0.10	0.87	...	...	...	...
$\Gamma$	$\lambda_{\text{Edd}}$	IIb	0.18	0.08	...	...	...	...
		III	0.15	0.12	...	...	...	...
		IV	0.15	0.12	...	...	...	...
		I	0.17	0.08	0.18	0.16	0.1	0.49
$E_{\text{cut}}$	$\Gamma$	IIa	...	...	...	...	...	...
		III	0.17	0.08	0.17	0.18	0.12	0.41
		I	0.69	1.75E-11	...	...	...	...
		IIa	0.99	1.46E-05	...	...	...	...
$\tau$	$kT_e$	IIb	0.57	0	...	...	...	...
		III	0.60	4.11E-12	...	...	...	...
		IV	0.61	1.75E-12	...	...	...	...
		I	-0.96	1.82E-23	...	...	...	...
$E_{\text{cut}}$	$\frac{M_{\text{BH}}}{M_{\text{Sun}}}$	IIa	-0.99	1.40E-24	...	...	...	...
		IIb	...	...	...	...	...	...
		III	-0.66	1.89E-10	...	...	...	...
		I	-0.02	0.86	...	...	...	...
$\Gamma$	$\frac{M_{\text{BH}}}{M_{\text{Sun}}}$	IIa	-0.54	0.27	...	...	...	...
		IIb	-0.08	0.38	...	...	...	...
		III	-0.20	0.04	...	...	...	...
		IV	-0.20	0.03	...	...	...	...
$\Gamma$	$\frac{M_{\text{BH}}}{M_{\text{Sun}}}$	I	-0.05	0.58	...	...	...	...
		IIa	...	...	...	...	...	...
		IIb	...	...	...	...	...	...
		III	-0.05	0.58	...	...	...	...

**Note.** Provided are the Spearman's rank correlation coefficient ( $\rho$ ) and the probability ( $p$ ) for the null hypothesis (no correlation). We fail to reject the null hypothesis if  $p$  is larger than 0.01. Here, Method I indicates the correlation study between two parameters with only uncensored values. Method IIa represents the correlation analysis performed between the median values of two parameters obtained from the survival analysis method using the nonparametric KMPL approach. Method IIb is the bivariate correlation analysis performed using the package ASURV. The correlation analysis between two parameters considering both uncensored (including the corresponding asymmetric errors) and censored values ( $E_{\text{cut}}^{\text{MAX}} = 1000$  keV,  $R^{\text{MIN}} = 0.01$ , and  $kT_e^{\text{MAX}} = 150$  keV) is denoted by Method III, wherein Method IV represents the same as Method III except the  $E_{\text{cut}}^{\text{MAX}}$  is considered to be 500 keV here.

rank correlation coefficient ( $\rho$ ) and the null hypothesis probability ( $p$ ) for no correlation. We considered a correlation to be significant if  $p$  was less than 0.01.

In the third approach, we incorporated the asymmetric errors related to the controlled  $E_{\text{cut}}$  measurements and the lower limits of  $E_{\text{cut}}$  by simulating  $10^5$  random points within the ranges of  $(E_{\text{cut}}^{\text{min}}, E_{\text{cut}}^{\text{max}})$  and  $(E_{\text{cut}}^{\text{LL}}, E_{\text{cut}}^{\text{MAX}})$ , respectively. For constrained  $E_{\text{cut}}$  with asymmetric errors,  $E_{\text{cut}}^{\text{min}}$  and  $E_{\text{cut}}^{\text{max}}$  represented the respective lower and upper bounds, while  $E_{\text{cut}}^{\text{LL}}$  denoted the lower limit obtained from the model fit. The  $10^5$  random points

were generated between the lower limit ( $E_{\text{cut}}^{\text{LL}}$ ) and a hypothetical upper bound ( $E_{\text{cut}}^{\text{MAX}}$ ) of 1000 keV. Following this approach, we calculated the median of  $E_{\text{cut}}$  for each run and then determined the mean of the median distribution. The statistical errors associated with the median values were calculated as the standard deviations of the  $10^5$  simulated median  $E_{\text{cut}}$  values.

In the fourth case, we handled the asymmetric errors corresponding to the constrained  $E_{\text{cut}}$  similarly as discussed in the third case. However, here, the upper bound  $E_{\text{cut}}^{\text{MAX}}$  was

set to 500 keV for cases where only lower limits were available. It was necessary to consider  $E_{\text{cut}}^{\text{MAX}} = 1000$  keV in three sources for which the lower limit of  $E_{\text{cut}}$  exceeded 450 keV. The median and standard deviation of each run were calculated, and the mean of their distributions was determined. In both cases, the linear relation was fitted (using Equation (2)) between  $E_{\text{cut}}$  and other parameters for each run, resulting in distributions of the slope ( $a$ ), the intercept ( $b$ ), the Spearman's rank correlation coefficient ( $\rho$ ), and the probability of no correlation ( $p$ ). The median values from these distributions were used to represent the best-fit values of the correlation. All values and errors for the unweighted and simulated correlations are presented in Table 1.

We followed a similar approach for the other parameters also ( $\Gamma$ ,  $R$ , and  $kT_e$ ), simulating  $10^5$  points between the minimum and maximum bounds for the correlation analysis. In the case of the reflection fraction ( $R$ ) and the coronal temperature ( $kT_e$ ), respective upper and lower limits were obtained. During the correlation analysis, the lower bound of  $R$  was set at 0.01, and the upper bound of  $kT_e$  was set at 150 keV.

Using the constrained values only, the median of  $E_{\text{cut}}$ , as obtained from Model 1, was  $104 \pm 8$  keV. The median of the unconstrained  $E_{\text{cut}}$  using the same model was  $173 \pm 18$  keV. Considering the upper limit of 1000 keV for the censored values and the asymmetric errors associated with the controlled  $E_{\text{cut}}$  measurements, we obtained a median of  $153 \pm 8$  keV for the full sample,  $158 \pm 11$  keV for the moderately accreting system ( $\lambda_{\text{Edd}} < 0.1$ ) and  $150 \pm 10$  keV for the systems with higher accretion ( $\lambda_{\text{Edd}} > 0.1$ ). Considering the upper limit of 500 keV, a median of  $151 \pm 7$  keV was obtained for the entire sample. For the moderate ( $\lambda_{\text{Edd}} < 0.1$ ) and high ( $\lambda_{\text{Edd}} > 0.1$ ) accreting systems, we obtained a median of  $152 \pm 10$  keV and  $147 \pm 10$  keV, respectively. Our result is consistent with the measurements of the median  $E_{\text{cut}}$  value obtained from the literature. For example, using a sample of unobscured Seyfert galaxies from the Swift-BAT 70 month catalog, C. Ricci et al. (2017) reported a median value of  $210 \pm 36$  keV, considering both censored and uncensored measurements. Using the XILLVER model to a total number of 195 Seyfert 1 galaxies, N. Kamraj et al. (2022) found a median  $E_{\text{cut}}$  of  $156 \pm 13$  keV.

We determined the median of  $kT_e$  as  $24 \pm 2$  keV and  $24 \pm 3$  keV, respectively, for the constrained and unconstrained best-fit values obtained using Model 2. Including the asymmetric errors and the lower limits by considering the upper bound of 150 keV, a median of  $48 \pm 5$  keV was obtained. The distribution of  $E_{\text{cut}}$  and  $kT_e$  (constraints and the lower limits) are given in Figures 2 and 4, respectively.

We also determined the median value of  $kT_e$  by analyzing a sample of 96 sources in common with both this study and that of C. Ricci et al. (2018). We obtained the estimate for  $E_{\text{cut}}$  from C. Ricci et al. (2018) and computed  $kT_e$  using Equation (1). The median value of  $kT_e$  for the subset with constrained values was  $27 \pm 7$  keV, consistent with our findings of the median for only the controlled measurements. For the unconstrained best-fit value of  $kT_e$ , as obtained from C. Ricci et al. (2018), the median was  $29 \pm 5$  keV. For 67 sources where only lower limits were reported in C. Ricci et al. (2018), we considered both the asymmetric errors associated with the best-fit  $E_{\text{cut}}$  and an upper limit of 500 keV for cases where only a lower limit was reported, yielding a median  $kT_e$  of  $85 \pm 6$  keV. This value is higher than what we observed for our sample but aligns with the results presented in N. Kamraj et al. (2022). The variance in

median  $kT_e$  values between this study and those in C. Ricci et al. (2018) may be attributed to the higher proportion of unconstrained  $E_{\text{cut}}$  values in the latter work. Additionally, setting an upper limit of 500 keV for unconstrained cases biases the median value toward higher temperatures. The distribution of  $kT_e$ , as calculated using Equation (1) based on  $kT_e$  values from C. Ricci et al. (2018), is illustrated in Figure 6.

### 5.1. Correlation between $E_{\text{cut}}$ and $\lambda_{\text{Edd}}$

We looked for a relation between  $E_{\text{cut}}$  and  $\lambda_{\text{Edd}}$ . Using all four methods of correlation analysis, we could not find any significant correlation between them. This is in agreement with recent results in the literature (A. Tortosa et al. 2018; M. Molina et al. 2019; J. T. Hinkle & R. Mushotzky 2021; N. Kamraj et al. 2022).

For AGN with moderate accretion ( $\lambda_{\text{Edd}} < 0.1$ ) (C. Ricci et al. 2018), the observed spectral energy distribution can be explained by the standard optically thick geometrically thin accretion disk with  $H/R < 1$ , where  $H$  is the height of the disk at a radius  $R$  (N. I. Shakura & R. A. Sunyaev 1973). But for AGN with higher  $\lambda_{\text{Edd}}$ , the accretion disk becomes geometrically thick with  $H \lesssim R$ , and therefore, the accretion flow nature is expected to differ from the moderately accreting ones (B. Paczynski & G. Bisnovaty-Kogan 1981; B. Muchotrzeb & B. Paczynski 1982; M. A. Abramowicz et al. 1988; J.-M. Wang et al. 2014; A. Tortosa et al. 2022). The emergent X-ray spectrum from AGN with thick and thin accretion disks is likely to be different, and hence, the connection between the accretion disk and corona in low and high accretion AGN could be different. To look for any differences in the corona between low and high accreting AGN, we divided our sample into moderately accreting AGN ( $\lambda_{\text{Edd}} < 0.1$ ) and highly accreting AGN ( $\lambda_{\text{Edd}} > 0.1$ ) and carried out linear fits to the data using Equation (2) in the  $E_{\text{cut}}$  versus  $\lambda_{\text{Edd}}$  plane. For the highly accreting subsample, we found no correlation between  $E_{\text{cut}}$  and  $\lambda_{\text{Edd}}$ , which is expected for the sources with higher accretion rates (J. M. Wang & H. Netzer 2003). From the Spearman's rank correlation test, we found a  $\rho$  of 0.41 and a  $p$  of 0.009 considering only the controlled best-fit values  $E_{\text{cut}}$  in the moderately accreting systems ( $\lambda_{\text{Edd}} < 0.1$ ), but including the asymmetric errors and taking the lower limits into consideration, we did not find any significant relation between these two parameters (see Table 1 and Figure 7). Due to a limited number of median data points in both regions, we could not perform a survival analysis test. Using the ASURV package, we obtained a  $\rho$  of 0.06 and a  $p$  of 0.55 for the entire sample; for the moderately accreting subsample, we obtained a  $\rho$  of 0.11 and a  $p$  of 0.39, and for the highly accreting subsample a  $\rho$  of  $-0.16$  and a  $p$  of 0.30 were calculated.

### 5.2. Correlation between $R$ and $\lambda_{\text{Edd}}$

We performed a simple linear fit to the data using Equation (2) to look for a correlation between  $R$  and  $\lambda_{\text{Edd}}$ . In a few cases, we could not constrain  $R$ ; rather, we found an upper limit. We considered both controlled values and the upper limits during the correlation analysis. Using only the controlled best-fit values, the Spearman's correlation analysis yielded a  $\rho$  of  $-0.28$  and a  $p$ -value of 0.01. The survival analysis using the KMPL test indicated no correlation between  $R$  and  $\lambda_{\text{Edd}}$  with  $\rho = -0.25$  and  $p = 0.05$ . Similar outcomes were also derived using the ASURV statistical analysis package. A Spearman's correlation coefficient of  $-0.22$  and  $p = 0.02$



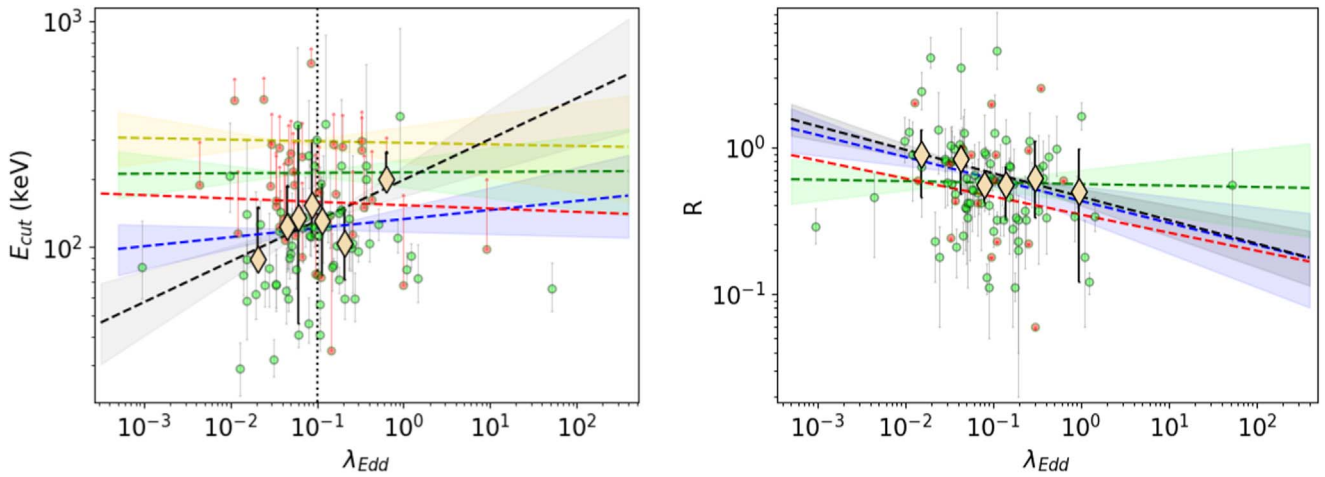


**Figure 7.** The relation between  $E_{\text{cut}}-\lambda_{\text{Edd}}$  (left panel) and  $R-\lambda_{\text{Edd}}$  (right panel). In the plots, the green dots denote the constrained values, and the red dots represent the lower/upper limits of the dependent parameters. In each panel, the blue dashed line is the linear fit to the constrained values, and the blue-shaded region indicates the errors in the slope and the intercept to the linear fit (Method I). The beige diamond points represent the median values of  $E_{\text{cut}}$  and  $R$  in each bin of  $\lambda_{\text{Edd}}$  obtained from the survival analysis using the KMPL approach. The black dashed line and the black shaded region are the linear fit and the errors in the fit parameters to the median values (Method II). The red dashed line represents the linear fit using the Schmitt method obtained using the package ASURV. The green dashed line and the shaded region represent the linear fit and the errors in the slope and the intercept for the linear relation fit between two parameters considering both uncensored (including the corresponding asymmetric errors) and censored (upper bound of  $E_{\text{cut}} = 500$  keV; lower bound of  $R = 0.01$ ) values (Method III) in each panel. The yellow dashed line and the shaded region in the first panel are the linear fit, and the errors in the fit parameters are similar to the green shaded region but considering the upper bound of  $E_{\text{cut}}$  to be 1000 keV (Method IV).

was obtained from the ASURV analysis. Using the third approach of the correlation analysis, we considered the asymmetric errors associated with the uncensored best-fit values of  $R$  and a lower bound of 0.01 in the cases where only the upper limit was found; we performed the linear fit  $10^5$  times. From the distribution of  $\rho$  and  $p$ , we obtained the median of  $\rho = -0.18$  and  $p = 0.07$ . We thus conclude that using both uncensored and censored values of  $R$ , we could not get a meaningful correlation between  $R$  and  $\lambda_{\text{Edd}}$ . For the sources with moderate ( $\lambda_{\text{Edd}} < 0.1$ ) and high ( $\lambda_{\text{Edd}} > 0.1$ ) accretion rates, we did not notice any significant correlation using Methods I and III. Due to limited median data points, we could not perform the survival analysis for separate accreting regions. Using the ASURV package, we obtained  $\rho = -0.25$  and  $p = 0.06$  for moderately accreting subsamples and  $\rho = -0.02$  and  $p = 0.88$  for highly accreting subsamples. Thus, considering our sample of objects and dividing them into two different accreting systems, we conclude that the relation between  $R$  and  $\lambda_{\text{Edd}}$  is insignificant (see Figure 7).

### 5.3. Correlation between $R$ and $\Gamma$

We obtained an indication of a positive correlation between  $\Gamma$  and the reflection fraction in Table 1. We used Equation (2) to perform a linear fit between these two parameters. The fit gave us a  $\rho$  of 0.30 and a  $p$  of 0.002, considering the controlled and upper limits of  $R$ . We obtained a positive correlation using only the constrained values with a  $\rho$  of 0.28 and a  $p$  of 0.009. However, the KMPL and ASURV survival analysis denied the correlation with a  $\rho$  of  $-0.55$  and  $0.59$  and a  $p$  of 0.26 and 0.03, respectively. The correlation is plotted in the left panel of Figure 8.

The study of the dependence of  $\Gamma$  on  $R$  has been done several times in the past (A. M. Beloborodov 1999; A. A. Zdziarski et al. 1999; J. Malzac et al. 2001; B. J. Mattson et al. 2007; M. Dadina 2008; M. Molina et al. 2009; R. Boissay et al. 2016; P. Lubiński et al. 2016; A. D. Moro et al. 2017; L. Zappacosta et al. 2018; C. Panagiotou & R. Walter 2019; S. H. Ezhikode et al. 2020; J. Kang et al. 2020). In most studies, the authors

found a strong correlation between  $R$  and  $\Gamma$ . Although B. J. Mattson et al. (2007) argued that this strong positive correlation could be due to the model degeneracies rather than any physical act, A. A. Zdziarski et al. (1999) suggested that the observed correlation could be explained by considering an internal feedback mechanism, where the medium emitting seed photons for the primary X-ray emission also serves as the medium for reflection. Recently, from the analysis of 14 nearby bright Seyfert galaxies, S. H. Ezhikode et al. (2020) confirmed a strong correlation between  $R$  and  $\Gamma$ . The authors argued that the observed correlation could be either due to the Compton cooling process or the changing geometry of the disk-corona system. Recently, J. Kang et al. (2020) also reported a strong correlation between  $R$  and  $\Gamma$ . According to the authors, a stronger reflection and a softer X-ray spectrum could be predicted in the case of an outflowing corona.

### 5.4. Correlation between $E_{\text{cut}}$ and $R$

We investigated the correlation between  $E_{\text{cut}}$  and  $R$ , performing the correlation analysis using the four methods mentioned above. Since the survival analysis with the ASURV package does not handle cases where the dependent variable has lower limits and the independent variable has upper limits simultaneously, we performed the survival analysis under the following conditions: (1) only the dependent variable ( $E_{\text{cut}}$ ) has a lower limit, (2) only the independent variable ( $R$ ) has an upper limit, and (3) both dependent and independent variables have detected points. From the correlation analysis using the above-described methods i.e., considering only the constrained best-fit values of  $E_{\text{cut}}$  and  $R$ ; using the survival analysis test (KMPL and ASURV package); considering the asymmetric errors and the constant upper and lower limits of  $E_{\text{cut}}^{\text{MAX}}$  to be 1000 keV and  $R^{\text{MIN}} = 0.01$  and  $E_{\text{cut}}^{\text{MAX}} = 500$  keV and  $R^{\text{MIN}} = 0.01$ , we obtained  $p = 0.84, 0.66, 0.08, 0.12,$  and  $0.12$  respectively, suggesting no significant correlation between these two parameters (see Figure 8). Previously, J. T. Hinkle & R. Mushotzky (2021) reported a mild anticorrelation between  $E_{\text{cut}}$  and  $R$ .

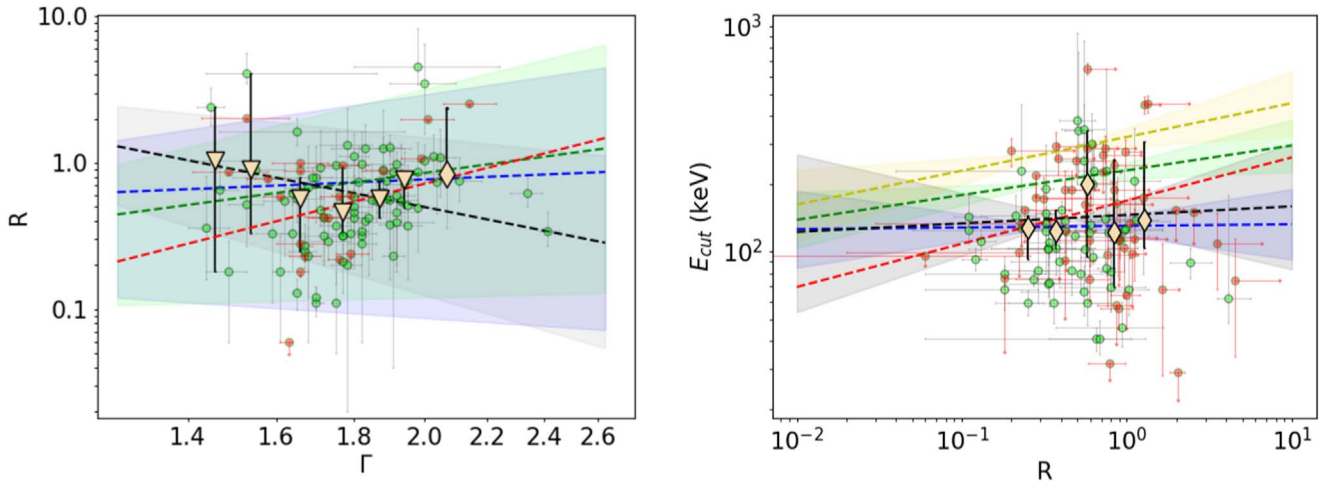


**Figure 8.** The relation between  $R$ – $\Gamma$  (left panel) and  $E_{\text{cut}}$ – $R$  (right panel). The descriptions of the lines and the shaded regions are the same as those in Figure 7.

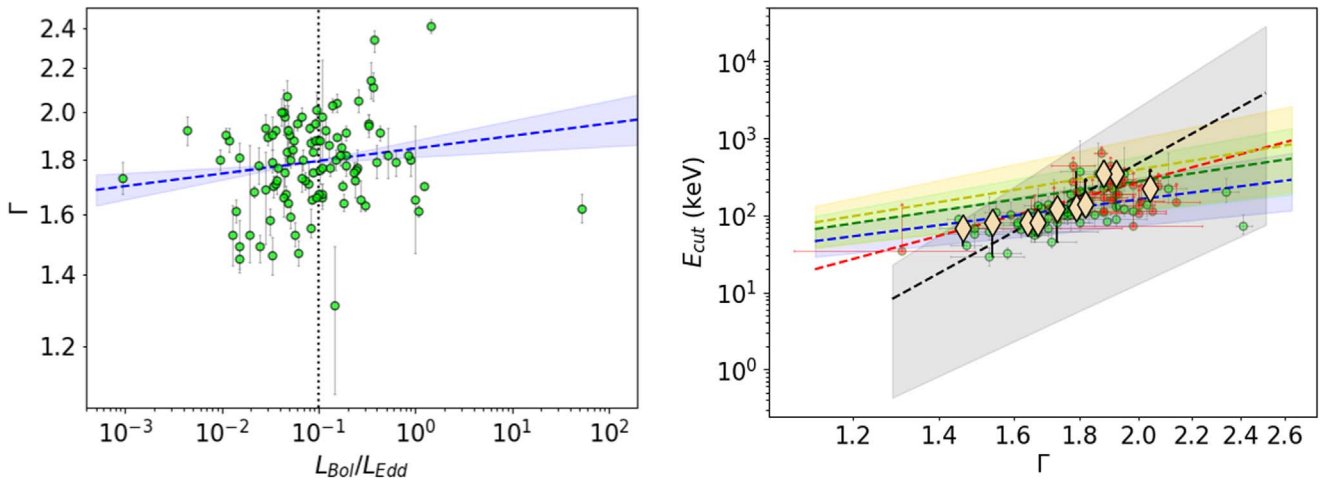


**Figure 9.** The relation between  $\Gamma$ – $\lambda_{\text{Edd}}$  (left panel) and  $E_{\text{cut}}$ – $\Gamma$  (right panel). The descriptions of the lines and the shaded regions are the same as those in Figure 7.

### 5.5. Correlation between $\Gamma$ and $\lambda_{\text{Edd}}$

Next, we examined the correlation between  $\Gamma$  and  $\lambda_{\text{Edd}}$ . Considering the whole sample, we noticed a positive trend, though insignificant, between these two parameters. The correlation analysis produced a  $\rho$  of 0.17 and a  $p$ -value of 0.08. We also conducted an analysis accounting for the errors in the measurements of  $\Gamma$ . Still, it did not yield any significant correlation, which agrees with what was reported by A. Tortosa et al. (2018). No significant correlation was found in the moderate ( $\lambda_{\text{Edd}} < 0.1$ ) and high ( $\lambda_{\text{Edd}} > 0.1$ ) Eddington ratio subsets. It is worth noting that previous studies (O. Shemmer et al. 2006, 2008; G. Risaliti et al. 2009; B. Trakhtenbrot et al. 2017; C. Ricci et al. 2018) have reported a positive correlation between these two parameters. The correlation is plotted in Figure 9.

### 5.6. Correlation between $E_{\text{cut}}$ and $\Gamma$

The correlation between  $E_{\text{cut}}$  and  $\Gamma$  is shown in Figure 9. From correlation analysis of the linear fit, we obtained a  $\rho$  of 0.69 and a  $p$ -value of  $1.75 \times 10^{-11}$  considering only the controlled measurements of  $E_{\text{cut}}$  and  $\Gamma$ , suggesting a significant correlation between these two parameters. The KMPL test of the survival analysis also indicated a strong correlation between  $E_{\text{cut}}$  and  $\Gamma$  with  $\rho = 0.99$  and  $p = 1.46 \times 10^{-5}$ . The statistical

analysis using the package ASURV derived a  $\rho = 0.57$  with  $p = 0.0$ , suggesting a strong correlation between these two parameters. Using the third approach, we found a  $\rho$  of 0.60 and a  $p$ -value of  $4.11 \times 10^{-12}$ . We also obtained a significant correlation between them using our fourth approach and got a  $\rho$  of 0.61 and a  $p$ -value of  $1.75 \times 10^{-12}$ . In the third and fourth cases, the errors in  $\Gamma$  are taken care of by producing  $10^5$  random points between  $\Gamma^{\text{min}}$  and  $\Gamma^{\text{max}}$  at each run, where  $\Gamma^{\text{min}}$  and  $\Gamma^{\text{max}}$  are the respective lower and upper bounds of  $\Gamma$ .

Similar studies on the correlation analysis between the temperature of the corona and  $\Gamma$  are available in the literature. From a study of 19 Seyfert galaxies using data from NuSTAR, A. Tortosa et al. (2018) found no significant correlation between  $kT_e$  and  $\Gamma$ . In contrast, M. Molina et al. (2019) found a positive correlation between  $E_{\text{cut}}$  and  $\Gamma$  based on spectral analysis of 18 Seyfert galaxies using data from Swift-XRT and NuSTAR. The authors suggested that the correlation observed in their sample could result from the systematic uncertainties affecting one of the two parameters or the lack of high-quality data in the soft X-ray regime. Several recent studies reported a positive correlation between  $E_{\text{cut}}$  and  $\Gamma$  (N. Kamraj et al. 2018; J. T. Hinkle & R. Mushotzky 2021; J.-L. Kang & J.-X. Wang 2022). Of these, N. Kamraj et al. (2018) analyzed a total of 46 Seyfert 1 galaxies, while J. T. Hinkle & R. Mushotzky (2021) and J.-L. Kang & J.-X. Wang (2022) carried out spectral

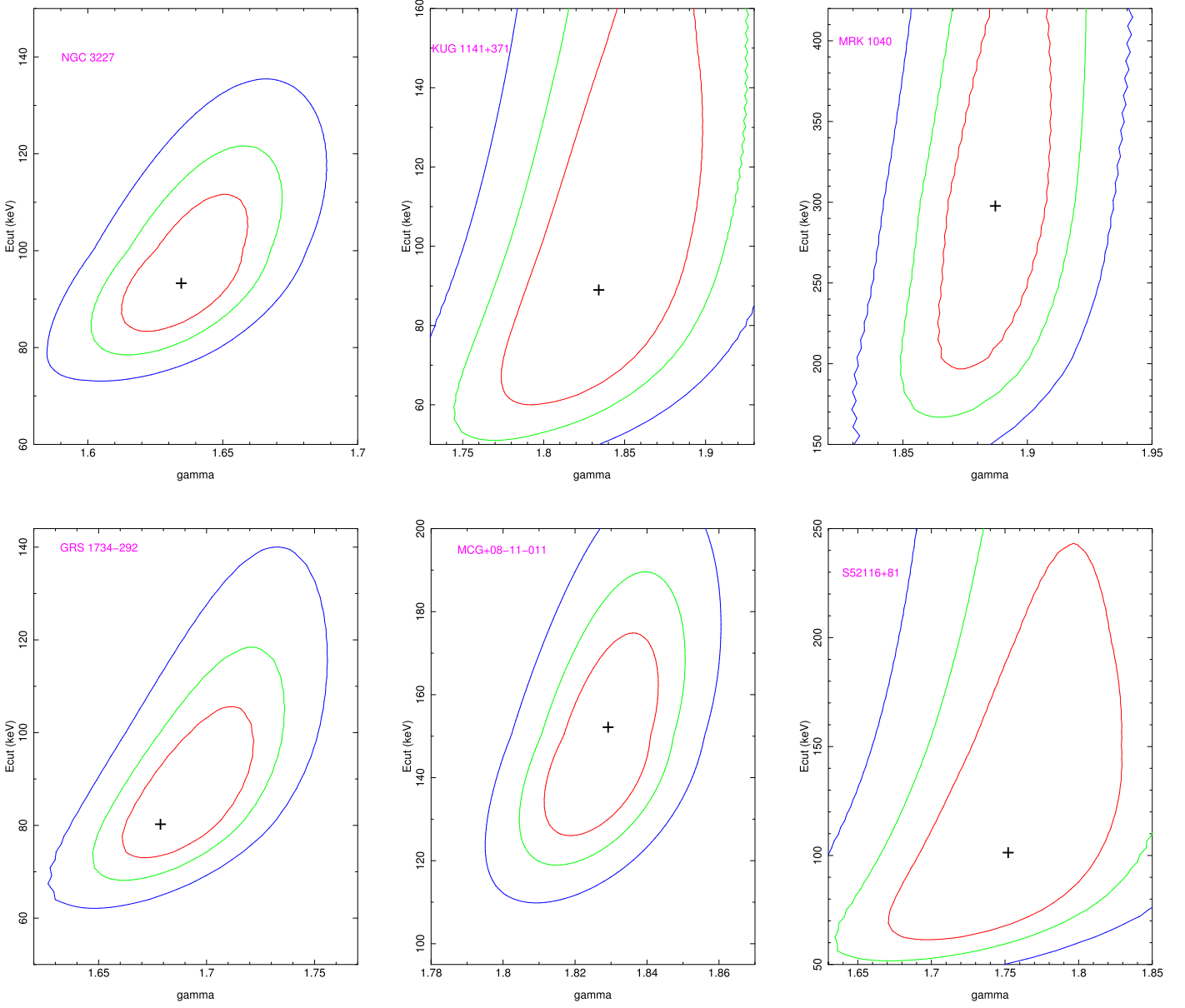


**Figure 10.** Confidence contours between  $E_{\text{cut}}$  and  $\Gamma$  obtained from Model 1 for six sources. The color codes for the contours are as follows: red, green, and blue for 68% ( $\Delta\chi^2 = 2.30$ ), 90% ( $\Delta\chi^2 = 4.61$ ), and 99% ( $\Delta\chi^2 = 11.8$ ) confidence levels, respectively. In each panel, the best-fit location is marked by the black plus sign.

analysis of 33 and 60 sources, respectively. While J.-L. Kang & J.-X. Wang (2022) found a relatively strong correlation between  $E_{\text{cut}}$  and  $\Gamma$ , it is rather weak, as reported in N. Kamraj et al. (2018) and J. T. Hinkle & R. Mushotzky (2021). This may be due to the small sample size and domination of the lower limits in the  $E_{\text{cut}}$  measurements in their studies. While our study produced a stronger correlation between these two parameters for a large number of sources in which we could tightly constrain  $\Gamma$  in all of them and  $E_{\text{cut}}$  in most of them, the influence of degeneracy between these two parameters could not be neglected. To check the degeneracy between  $E_{\text{cut}}$  and  $\Gamma$  in our sample, we generated contours between these two parameters for all the sources, six of which are presented in Figure 10. The contours are elliptical and have smooth levels, suggesting the parameters were well-constrained. While we noticed weak degeneracy in the contour plots, we managed to constrain both parameters effectively in the majority of cases. This implies that any potential artifacts between

them may be minor, given the substantial number of sources analyzed in this study.

From an analysis of multiple epochs of observations on the source SWIFT J2127.4+5654, J.-L. Kang et al. (2021) found a  $\Lambda$ -shaped pattern. According to the authors, up to  $\Gamma < 2.05$ , the source showed a “steeper-when-hotter” behavior, while beyond  $\Gamma > 2.05$ , the source showed a “softer-when-cooler” behavior. Though the finding of J.-L. Kang et al. (2021) is from multiple observations of a single source, we attempted to check the prevalence of such a trend in our sample of sources. There are only a few sources in our sample with  $\Gamma > 2.05$ , and the statistical test resulted in a negative trend between  $E_{\text{cut}}$  and  $\Gamma$ . However, we could not draw any conclusions regarding the significance of the anticorrelation noticed since very few sources were found in the  $\Gamma > 2.05$  region. A systematic and homogeneous analysis of many sources is needed to confirm this finding.

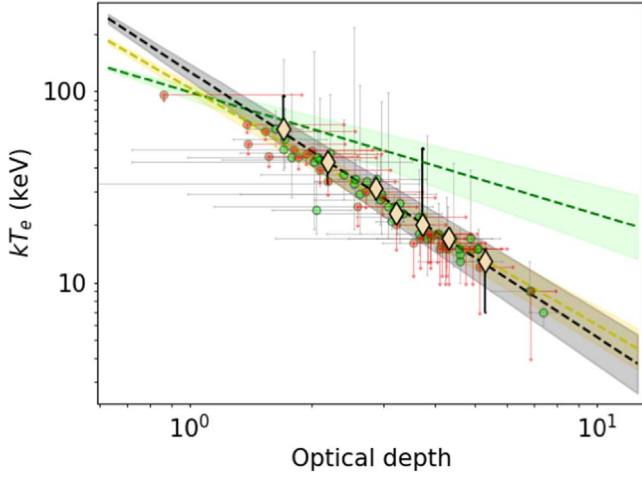


**Figure 11.** The relation between  $kT_e$  and  $\tau$ . The green dots are the constrained values of the parameters, and the red dots denote the lower and upper limits of  $kT_e$  and  $\tau$ , respectively. The yellow dashed line and the yellow shaded region are the linear fits to the constrained values of  $kT_e$  and  $\tau$ , and the errors in the slope and the intercept of the linear fit (Method I). The beige-filled diamond points represent the median values of  $kT_e$  in each bin of  $\tau$  obtained from the survival analysis using the KMPL approach. The black dashed line and the black shaded region are the linear fit and the errors in the fit parameters to the median values of  $kT_e$  (Method II). The green dashed line and the green shaded region represent the linear fit and the errors in the slope and the intercept for the fit between two parameters considering both uncensored (including the corresponding asymmetric errors in  $kT_e$ ) and censored (upper bound of  $kT_e = 150$  keV) values of two parameters (Method III).

### 5.7. Correlation between $kT_e$ and $\tau$

We calculated  $\tau$  using the following equation (A. A. Zdziarski et al. 1996; P. T. Życki et al. 1999):

$$\tau = \sqrt{\frac{9}{4} + \frac{3}{\theta \left[ \left( \Gamma + \frac{1}{2} \right)^2 - \frac{9}{4} \right]}} - \frac{3}{2}, \quad (3)$$

where  $\theta = kT_e/m_e c^2$ . Considering only the constrained values of  $kT_e$ , we found a strong negative correlation between  $kT_e$  and  $\tau$  (see Figure 11). A Spearman's rank correlation analysis yielded a  $\rho$  of  $-0.96$  with a  $p$ -value of  $1.82 \times 10^{-23}$ . Earlier, A. Tortosa et al. (2018) also found a strong anticorrelation between these parameters for slab and spherical geometries. The authors fitted a similar linear relation in the  $kT_e$  versus  $\tau$  plane and reported that

$$a = -0.7 \pm 0.2; b = 1.8 \pm 0.1 \quad (4)$$

for the spherical geometry. We also found similar values of  $a$  and  $b$  from our linear fit to the data points,

$$a = -1.24 \pm 0.07; b = 2.02 \pm 0.03. \quad (5)$$

From the survival analysis, we obtained a  $\rho$  of  $-0.99$  and  $p = 1.40 \times 10^{-24}$ , indicating a strong anticorrelation between these two parameters. We could not perform the statistical test using the ASURV package since it does not calculate the correlation when the dependent variable ( $kT_e$ ) has a lower limit, and the independent variable ( $\tau$ ) has an upper limit simultaneously. Using an upper limit of 150 keV for unconstrained  $kT_e$ , we confirmed a strong negative correlation between  $kT_e$  and  $\tau$  with a  $\rho$  of  $-0.66$  and  $p = 1.89 \times 10^{-10}$  (see Table 1).

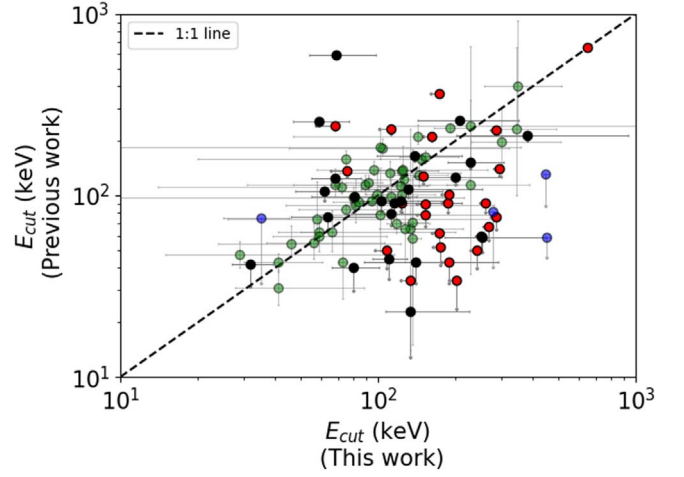


**Figure 12.** Plot of the estimated  $E_{\text{cut}}$  values from this work and those obtained from the literature. The green dots indicate the constrained  $E_{\text{cut}}$  values obtained from both this study and prior research. The red dots signify the lower limits of  $E_{\text{cut}}$  values derived from both this study and the existing literature. The black dots denote the constrained  $E_{\text{cut}}$  values from this study and the lower limits of  $E_{\text{cut}}$  from the literature. The blue dots represent the constrained  $E_{\text{cut}}$  values from the literature and the lower limits of  $E_{\text{cut}}$  values from this study. The 1:1 line is also shown (the black dotted line) for reference.

## 6. Comparison with Previous Work

This section compares the best-fit values of  $E_{\text{cut}}$  from this work with those available in the literature. Of the 112 sources analyzed in this work, we could constrain  $E_{\text{cut}}$  for 73 sources. For all these 112 sources,  $E_{\text{cut}}$  measurements were carried out using the most recent physical models (XILLVER/RELXILL/(RELXILL+XILLVER)) available. In the past, most of these nearby unobscured AGN were analyzed vividly using mostly phenomenological models such as PEXRAV/PEXMON, etc. Here, we present a comparison of the  $E_{\text{cut}}$  measurements obtained from our analysis with those available in the literature in Table 3.

For the majority of the sources in literature,  $E_{\text{cut}}$  was reported using the broadband spectral analysis of the NuSTAR data in conjunction with the soft X-ray data from several other instruments, such as XMM-Newton, Swift-XRT, etc. (A. C. Fabian et al. 2015; T. J. Turner et al. 2018; M. Molina et al. 2019; J. T. Hinkle & R. Mushotzky 2021; D. Porquet et al. 2021; N. Kamraj et al. 2022; Y. Diaz et al. 2023). In several references,  $E_{\text{cut}}$  was obtained from the analysis of the Swift-BAT, BeppoSAX, and INTEGRAL broadband X-ray data (M. Dadina 2007; C. Ricci et al. 2017; M. Molina et al. 2013; A. Malizia et al. 2014). As seen in Table 3, our results from the analysis of only the NuSTAR data agree with the previous analysis (see Figure 12). Our derived  $E_{\text{cut}}$  also matches with those already reported in the literature using only the NuSTAR data (N. Kamraj et al. 2018; A. Tortosa et al. 2018; M. Baloković et al. 2020; S. H. Ezhikode et al. 2020; J. Kang et al. 2020; A. Akylas & I. Georgantopoulos 2021). Since these sources are known to be variable, we noticed a mismatch in the  $E_{\text{cut}}$  values in a few cases where the epoch of observations differs from those used in this work. In Figure 12, we plotted the constrained  $E_{\text{cut}}$  values obtained from both this work and the previous work with green dots; the red dots represent the lower limit of  $E_{\text{cut}}$  from both this work and the literature. The black ones represent the constrained  $E_{\text{cut}}$  from this work and the lower limit of  $E_{\text{cut}}$  from the literature. Finally, we plotted the constrained  $E_{\text{cut}}$  from the literature and the lower limit of  $E_{\text{cut}}$  values from this

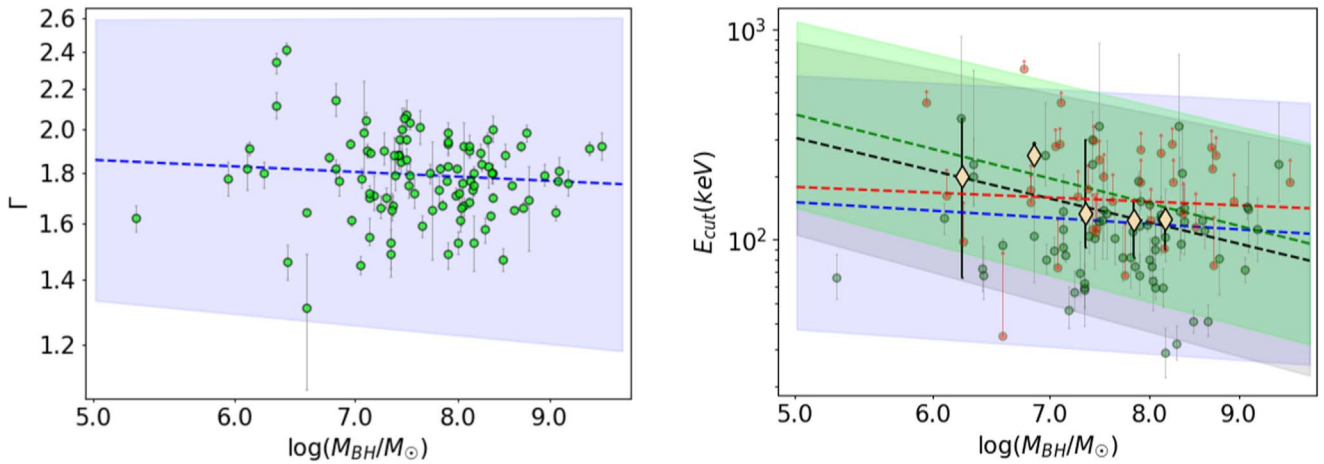


**Figure 13.** The relation between  $\Gamma$  and  $E_{\text{cut}}$  with the black hole mass. The descriptions of the lines and the shaded regions are the same as the descriptions given in Figure 7.

work using blue dots. The gray lines indicated the errors and the lower limits. Most of the sources lie around the 1:1 line (black dotted line), except for a few red dots, representing the lower limit obtained from this work is lower than that found in the literature.

## 7. Discussion

We examined the correlations between various coronal properties, as well as between coronal parameters and the physical properties of the sources studied in this work. We also examined whether moderately accreting sources ( $\lambda_{\text{Edd}} < 0.1$ ) have different X-ray emission characteristics relative to the highly accreting sources ( $\lambda_{\text{Edd}} > 0.1$ ).

From Table 1, we noticed a significant correlation between  $E_{\text{cut}}$  and  $\Gamma$  (see Figure 9) for the entire sample of sources. Such a positive correlation between  $E_{\text{cut}}$  and  $\Gamma$  has also been reported in the past (G. C. Perola et al. 2002; N. Kamraj et al. 2018; R. Middei et al. 2019; J. T. Hinkle & R. Mushotzky 2021; J.-L. Kang & J.-X. Wang 2022). However, there are instances where the observed correlation between  $E_{\text{cut}}$  and  $\Gamma$  was not definitively established (M. Molina et al. 2009; C. Ricci et al. 2017; A. Tortosa et al. 2018; N. Kamraj et al. 2022). According to R. Middei et al. (2019), the observed correlation might result from potential systematic uncertainties associated with one of the two parameters. The observed correlation could also be accounted for by the presence of an optically thin corona. Furthermore, the relationship between these two variables remains incomprehensible even for individual AGN (J.-L. Kang et al. 2021).

From our analysis, another strong anticorrelation was found between  $kT_e$  and  $\tau$  (see Figure 11). Such a negative correlation between  $kT_e$  and  $\tau$  is already known in literature and is attributed to either the fact that the cooling rate is more efficient in corona with higher opacity or to the variation in the intrinsic disk emission from the sources (A. Tortosa et al. 2018; J.-L. Kang & J.-X. Wang 2022). The positive correlation between  $E_{\text{cut}}$  and  $\Gamma$  suggests that a steeper spectrum typically corresponds to a hotter corona. The corona must become optically thinner for a spectrum to steepen, indicating a hotter environment. Consequently, the inverse correlation between  $kT_e$  and  $\tau$  indicates that a sustainable, hotter corona has lower opacity and a softer spectrum. These findings challenge the traditional notion that a corona in a higher accreting system tends to be cooler due to its rapid interaction with the seed disk

photons, resulting in a softer X-ray spectrum. Therefore, the observed correlation is likely driven by variations in the intrinsic disk emission across different sources.

We therefore examined the correlations between  $E_{\text{cut}}$  and  $\Gamma$  with the physical parameters of the sources ( $\lambda_{\text{Edd}}$  and  $M_{\text{BH}}$ ) (see Table 1 and Figure 13). In the past, several authors have reported a positive correlation between  $\Gamma$  and  $\lambda_{\text{Edd}}$  (W. N. Brandt et al. 1997; O. Shemmer et al. 2006, 2008; G. Risaliti et al. 2009; M. Brightman et al. 2013, 2016; B. Trakhtenbrot et al. 2017). Most authors have utilized a linear relationship similar to that described in Equation (2) to investigate the connection between these two parameters. We found a slope ( $b$ ) of 0.26, with a  $\rho$ -value of 0.17 and a  $p$ -value of 0.08 from Spearman’s correlation analysis. Our findings align with the slope reported by O. Shemmer et al. (2008) and M. Brightman et al. (2013), both of whom identified a similar slope of approximately 0.3 from the correlation analyses between  $\Gamma$  and  $\lambda_{\text{Edd}}$ . However, G. Risaliti et al. (2009), in their examination of Sloan Digital Sky Survey (SDSS) quasars with archival XMM-Newton observations, reported a steeper slope ( $b \sim 0.6$ ). More recently, B. Trakhtenbrot et al. (2017) employed BASS data and found a considerably weaker and flatter correlation ( $b \sim 0.15$ ). B. Trakhtenbrot et al. (2017) argued that as  $M_{\text{BH}}$  decreases, the number of optical/UV seed photons increases and due to the production of a larger amount of seed photons, the corona interacts with it rapidly, and that in turn cools the corona down, resulting in a softer spectrum. Therefore, based on this argument, one should expect a positive correlation between  $\Gamma$  and  $M_{\text{BH}}$ . From the analysis of our sample of sources, we could not confirm such a trend. We also explored the relationship between  $E_{\text{cut}}$  and  $\lambda_{\text{Edd}}$ . When analyzing the entire sample, as well as the higher and lower accretion regimes separately, no significant correlation was observed between these two parameters. These findings are consistent with similar results reported in the literature (A. Tortosa et al. 2018; R. Middei et al. 2019; J. T. Hinkle & R. Mushotzky 2021; N. Kamraj et al. 2022). Additionally, we did not find any significant correlation between  $E_{\text{cut}}$  and  $M_{\text{BH}}$ . Therefore, the lack of significant correlations between the coronal parameters and the physical properties of the sources suggests that the observed significant correlation between  $E_{\text{cut}}$  and  $\Gamma$ , with  $\tau$  decreasing significantly as  $kT_e$  increases, may not be due to intrinsic changes in the sources themselves or due to

the Compton cooling effect (i.e., cooler corona has steeper spectrum), but rather due to morphological variations in the corona across different sources. A larger data set is needed to better understand the nature of these observed correlations.

## 8. Summary

In this study, we analyzed the 3–79 keV NuSTAR spectra of a sample of 112 Seyfert 1 galaxies, the data for which were publicly available between 2013 August and 2022 May in the NuSTAR Master Catalog. The motivation is to carry out a systematic study of the coronal properties of Seyfert 1 type AGN. From the physical model fits to the spectrum of 112 sources, we could constrain  $E_{\text{cut}}$  in 73 sources. We used physically motivated Comptonization models to derive various physical coronal properties. We could constrain  $kT_e$  in 42 sources. The results of this study are summarized below:

1. Using Model 1, we estimated the median value of  $\Gamma$  to be  $1.79 \pm 0.02$ . Using Model 2, we derived a median of  $1.86 \pm 0.01$  for  $\Gamma$ .
2. The median values, as calculated using Model 1, were  $104 \pm 8$  keV and  $173 \pm 18$  keV for the best-fitted constrained and unconstrained values of  $E_{\text{cut}}$ , respectively. When considering an upper limit of 1000 keV for the censored  $E_{\text{cut}}$  measurements and accounting for the asymmetric errors in the constrained  $E_{\text{cut}}$  values, the median value for  $E_{\text{cut}}$  across the entire sample was determined to be  $153 \pm 8$  keV. In the subsample with moderate accretion rates ( $\lambda_{\text{Edd}} < 0.1$ ), the median  $E_{\text{cut}}$  was found to be  $158 \pm 11$  keV, while in the subsample with high accretion rates ( $\lambda_{\text{Edd}} > 0.1$ ), the median  $E_{\text{cut}}$  is  $150 \pm 10$  keV.
3. The median values of constrained and unconstrained  $kT_e$ , as estimated using Model 2, were  $24 \pm 2$  keV and  $24 \pm 3$  keV, respectively. Using both the controlled and censored  $kT_e$  (considering an upper bound of 150 keV), the median value of  $kT_e$  was calculated to be  $48 \pm 5$  keV.
4. For our sample of sources, we found  $E_{\text{cut}}$  is strongly correlated with  $kT_e$  as  $E_{\text{cut}} = (3.80 \pm 0.53)kT_e + (8.15 \pm 16.51)$ . This is in agreement with the notion that the X-ray spectra of AGN are related to the temperature of the corona as  $E_{\text{cut}} = 2-3kT_e$ . However, a large number of sources analyzed in this work lie above the  $E_{\text{cut}} = 3kT_e$

line, which is a deviation from the general notion of  $E_{\text{cut}} = 2-3kT_e$ . Analysis of more sources is needed to confirm this.

5. For our entire sample, we found a strong correlation between  $E_{\text{cut}}$  and  $\Gamma$ .
6. We found a significant anticorrelation between  $kT_e$  and  $\tau$ . The best-fit relation yielded a slope and intercept of  $-1.24 \pm 0.07$  and  $2.02 \pm 0.03$ .
7. All these correlations indicate that an optically thin corona is necessary to sustain a hotter corona with a steeper spectrum. With the increasing accretion rate, the hotter corona could move vertically away from the central engine and become optically thinner. A systematic and homogeneous analysis of a larger sample of sources is needed to establish the correlation observed between various physical quantities, thereby enhancing our understanding of AGN corona.

## Acknowledgments

We thank the anonymous referee for their very helpful comments on the manuscript. We thank the NuSTAR Operations, Software and Calibration teams for support with the execution and analysis of these observations. This research has made use of the NuSTAR Data Analysis Software (NuSTARDAS) jointly developed by the ASI Science Data Center (ASDC, Italy) and the California Institute of Technology (USA). C.R. acknowledges support from the Fondecyt Regular (grant 1230345) and ANID BASAL (project FB210003). This research has used data and/or software provided by the High Energy Astrophysics Science Archive Research Center (HEASARC), a service of the Astrophysics Science Division at NASA/GSFC.

*Facility:* NuSTAR

*Software:* FTOOLS.<sup>16</sup>

## Appendix A

### Additional Tables Containing Information on the Sources

In Appendix A, we provide information on each source (Table 2) and present the best-fit results from fitting their spectra using Model 1 and Model 2 (Tables 3 and 4, respectively).

<sup>16</sup> <https://heasarc.gsfc.nasa.gov/ftools/>



**Table 2**  
(Continued)

Source	$\alpha_{2000}$ R.A. (hh:mm:ss)	$\delta_{2000}$ Decl. (deg: mm: ss)	$z$	Type	Obs ID	Count Rate (counts $s^{-1}$ )	Exposure (s)	$M_{BH}/M_{\odot}$	$L_{bol}/L_{edd}$
MRK 1383	14 29 06.57	+01 17 06.15	0.086	Sy1.0	60501049002	0.18	95,955	8.67	0.04
MRK 1392	15 05 56.55	+03 42 26.33	0.036	Sy1.0	60160605002	0.14	21,084	7.9	0.03
MRK 1393	15 08 53.95	-00 11 49.00	0.054	Sy1.5	60376005002	0.21	30,816	7.42	0.32
MRK 205	12 21 44.07	+75 18 38.24	0.071	Sy1.0	60160490002	0.21	20,372	8.11	0.12
Mrk 279	13 53 03.43	+69 18 29.41	0.031	Sy1.5	60601011004	0.16	200,632	7.89	0.02
MRK 290	15 35 52.40	+57 54 09.51	0.03	Sy1.0	60061266004	0.2	26,348	7.64	0.05
MRK 335	00 06 19.53	+20 12 10.61	0.025	Sy1.2	60001041005	0.17	93,022	7.08	0.11
MRK 359	01 27 32.52	+19 10 43.83	0.017	Sy1.5	60402021002	0.15	52,526	6.11	0.43
Mrk 509	20 44 09.75	-10 43 24.72	0.034	Sy1.5	60101043002	1.19	165,885	8.13	0.13
MRK 590	02 14 33.56	-00 46 00.18	0.026	Sy1.2	80502630002	0.33	68,123	8.12	0.02
MRK 595	02 41 34.87	+07 11 13.85	0.027	Sy1.5	60160119002	0.06	21,298	6.58	0.15
MRK 684	14 31 04.78	+28 17 14.12	0.045	Sy1.0	60160586002	0.08	20,497	6.83	0.34
MRK 704	09 18 25.99	+16 18 19.63	0.029	Sy1.5	60061090002	0.27	21,524	8.35	0.01
MRK 732	11 13 49.75	+09 35 10.58	0.029	Sy1.5	60061208002	0.21	26,359	7.06	0.19
MRK 79	07 42 32.82	+49 48 34.78	0.022	Sy1.2	60601010002	0.58	65,805	7.48	0.13
MRK 813	14 27 25.05	+19 49 52.26	0.11	Sy1.0	60160583002	0.21	24,562	8.73	0.07
MRK 817	14 36 22.08	+58 47 39.39	0.031	Sy1.5	60601007002	0.21	135,300	7.74	0.99
MRK 841	15 04 01.19	+10 26 15.78	0.036	Sy1.5	60101023002	0.44	23,419	8.16	0.05
MRK 876	16 13 57.18	+65 43 09.95	0.121	Sy1.0	60160633002	0.1	29,969	9.11	0.02
MRK 885	16 29 48.38	+67 22 41.98	0.025	Sy1.5	60160641002	0.08	28,304	7.27	0.03
MRK 915	22 36 46.50	-12 32 42.89	0.024	Sy1.0	60002060004	1.53	54,249	7.13	0.07
MRK 926	23 04 43.48	-08 41 08.62	0.047	Sy1.5	60201029002	1.53	106,201	8.37	0.18
Mrk739E	11 36 29.30	+21 35 45.00	0.03	Sy1.0	60260008002	0.12	18,547	7.48	0.05
NGC 0985	02 34 37.88	-08 47 17.02	0.043	Sy1.0	60761008002	0.39	21,326	8.25	0.05
NGC 3227	10 23 30.57	+19 51 54.28	0.004	Sy1.5	60202002002	0.96	49,800	6.58	0.05
NGC 3516	11 06 47.46	+72 34 07.29	0.009	Sy1.5	60002042004	0.17	72,088	7.11	0.01
NGC 3783	11 39 01.71	-37 44 19.00	0.009	Sy1.0	60101110002	1.11	41,265	7.13	0.08
NGC 4051	12 03 09.61	+44 31 52.68	0.002	Sy1.5	60401009002	0.43	311,139	5.95	0.02
NGC 4579	12 37 43.52	+11 49 05.49	0.005	Sy1.9	60201051002	0.17	117,843	7.8	0.00
NGC 4593	12 39 39.44	-05 20 39.03	0.008	Sy1.0	60001149002	0.63	23,317	6.77	0.08
NGC 5273	13 42 08.38	+35 39 15.46	0.004	Sy1.9	60061350002	0.46	21,117	6.42	0.03
NGC 5548	14 17 59.54	+25 08 12.60	0.016	Sy1.5	60002044006	0.99	51,460	7.97	0.04
NGC 7469	23 03 15.67	+08 52 25.28	0.017	Sy1.2	60101001002	0.75	21,579	7.48	0.09
NGC 931	02 28 14.46	+31 18 41.46	0.017	Sy1.0	60101002004	0.74	64,242	7.41	0.09
PG 0026+129	00 29 13.70	+13 16 03.94	0.142	Sy1.0	60663003002	0.19	147,374	7.82	0.85
PG 0052+251	00 54 52.11	+25 25 38.98	0.155	Sy1.2	60661001002	0.13	24,392	8.7	0.09
PG 0804+761	08 10 58.66	+76 02 42.45	0.101	Sy1.0	60160322002	0.18	17,315	7.9	0.33
RBS 1037	11 49 18.68	-04 16 50.79	0.085	Sy1.0	60061215002	0.1	40,679	8.36	0.04
RBS 0295	02 14 37.40	-64 30 05.06	0.074	Sy1.0	60061021002	0.13	23,366	8.15	0.07
RBS 0770	09 23 43.00	+22 54 32.57	0.033	Sy1.2	60602018002	0.57	42,960	7.34	0.27
S52116+81	21 14 01.17	+82 04 48.35	0.084	Sy1.0	60061303002	0.36	18,542	8.16	0.23
SDSS J114921.52+532013.4	11 49 21.53	+53 20 13.29	0.095	Sy1.0	60260009002	0.06	24,886	8.16	0.01
SDSS J104326.47+110524.2	10 43 26.47	+11 05 24.26	0.047	Sy1.0	60376004002	0.13	31,062	8.01	0.04
SWIFT J2127.4+5654	21 27 45.39	+56 56 34.91	0.0147	Sy1.0	60001110005	0.712	74,578	7.15	0.15
UGC 10120	15 59 09.62	+35 01 47.56	0.031	Sy1.0	60560027002	0.05	62,881	...	...
UGC 3478	06 32 47.17	+63 40 25.28	0.013	Sy1.2	60061068002	0.13	21,680	...	...
UGC 03601	06 55 49.53	+40 00 01.12	0.017	Sy1.5	60160278002	0.1	19,674	7.33	0.02
UGC 06728	11 45 15.94	+79 40 53.37	0.067	Sy1.2	60160450002	0.14	22,615	5.28	51.96
VII ZW 653	16 25 25.95	+85 29 41.69	0.063	Sy1.0	60160639002	0.14	27,580	7.46	0.26
VII ZW 742	17 46 59.94	+68 36 39.59	0.063	Sy1.0	60160676004	0.05	31,393	7.37	0.10

**Note.** Some of the information, including the R.A., decl., and  $z$ , are from SIMBAD (<http://simbad.cds.unistra.fr/simbad/>).



**Table 3**  
Best-fit Parameters to the Source Spectra Obtained from the Model CONST  $\times$  TBABS  $\times$  ZTBABS  $\times$  (XILLVER/RELXILL/(RELXILL+XILLVER))

Source	$\Gamma$	$E_{\text{cut}}$ (keV)	$R$	$\chi^2/\text{dof}$	$E_{\text{cut}}$ from the Literature	References
1H 0419-577	$1.67^{+0.03}_{-0.04}$	$59^{+8}_{-7}$	$0.25^{+0.06}_{-0.06}$	1318/1255	$83^{+78}_{-31}$ $63^{+8}_{-9}$ $49^{+7}_{-5}$	C. Ricci et al. (2017) T. J. Turner et al. (2018) N. Kamraj et al. (2022)
1H1934-063	$2.34^{+0.05}_{-0.06}$	$200^{+102}_{-52}$	$0.62^{+0.17}_{-0.12}$	1223/1215	$\geq 126$	C. Ricci et al. (2017)
2E1739.1-1210	$1.89^{+0.04}_{-0.03}$	$>286$	$0.57^{+0.29}_{-0.17}$	443/405	$\geq 230$	C. Ricci et al. (2017)
2MASS J18302317+731310	$1.44^{+0.05}_{-0.04}$	$59^{+14}_{-11}$	$0.36^{+0.45}_{-0.20}$	298/280	$60^{+49}_{-20}$	A. Akylas & I. Georgantopoulos (2021)
2MASS J17485512-3254521	$1.61^{+0.04}_{-0.04}$	$75^{+18}_{-14}$	$<0.59$	414/427	$159^{+66}_{-55}$	C. Ricci et al. (2017)
2MASX J04372814-4711298	$1.98^{+0.05}_{-0.05}$	$116^{+96}_{-38}$	$0.87^{+0.49}_{-0.38}$	272/297	$\geq 91$ $>142$	C. Ricci et al. (2017) A. Akylas & I. Georgantopoulos (2021)
2MASX J11324928+1017473	$2.00^{+0.10}_{-0.10}$	$>108$	$3.50^{+3.00}_{-1.93}$	63/58	$\geq 50$	C. Ricci et al. (2017)
2MASX J12313717-4758019	$1.88^{+0.06}_{-0.06}$	$>112$	$<0.89$	136/178	$\geq 231$	C. Ricci et al. (2017)
2MASX J15295830-1300397	$1.79^{+0.05}_{-0.05}$	$>201$	$<0.60$	224/214	$\geq 34$	C. Ricci et al. (2017)
2MASX J1802473-145454	$1.72^{+0.06}_{-0.06}$	$133^{+165}_{-52}$	$0.32^{+0.09}_{-0.11}$	603/569	$\geq 74$ $66^{+36}_{-18}$	C. Ricci et al. (2017) A. Akylas & I. Georgantopoulos (2021)
2MASX J18470283-7831494	$1.80^{+0.04}_{-0.04}$	$122^{+60}_{-36}$	$0.59^{+0.49}_{-0.24}$	250/276	$\geq 93$	C. Ricci et al. (2017)
2MASX J18560128+1538059	$1.47^{+0.04}_{-0.04}$	$41^{+5}_{-5}$	$0.65^{+0.40}_{-0.31}$	287/307	$43^{+20}_{-11}$	A. Akylas & I. Georgantopoulos (2021)
2MASX J19380437-5109497	$1.85^{+0.05}_{-0.05}$	$102^{+64}_{-29}$	$0.56^{+0.42}_{-0.34}$	243/255	$78^{+191}_{-42}$ $>195$	C. Ricci et al. (2017) N. Kamraj et al. (2022)
2MASX J21192912+3332566	$1.80^{+0.04}_{-0.04}$	$82^{+33}_{-18}$	$0.46^{+0.36}_{-0.27}$	351/344	$62^{+150}_{-32}$ $89^{+199}_{-38}$	C. Ricci et al. (2017) A. Akylas & I. Georgantopoulos (2021)
2MASX J21355399+4728217	$1.66^{+0.05}_{-0.04}$	$56^{+15}_{-10}$	$<0.89$	287/292	$67^{+96}_{-23}$ $55^{+50}_{-19}$	C. Ricci et al. (2017) A. Akylas & I. Georgantopoulos (2021)
2MASX J23013626-5913210	$1.68^{+0.06}_{-0.06}$	$41^{+8}_{-6}$	$0.68^{+0.62}_{-0.62}$	174/179	$31^{+47}_{-13}$ $59^{+150}_{-26}$	C. Ricci et al. (2017) N. Kamraj et al. (2022)
3C 109	$1.64^{+0.03}_{-0.03}$	$72^{+10}_{-9}$	$0.33^{+0.21}_{-0.15}$	587/627	$\geq 115$ $112^{+62}_{-58}$	C. Ricci et al. (2017) J. T. Hinkle & R. Mushotzky (2021)
3C 111	$1.75^{+0.01}_{-0.01}$	$124^{+13}_{-16}$	$0.11^{+0.07}_{-0.06}$	910/890	$\geq 144$ $136^{+47}_{-29}$	C. Ricci et al. (2017) A. Malizia et al. (2014)
3C 120	$1.82^{+0.01}_{-0.01}$	$147^{+12}_{-9}$	$0.32^{+0.04}_{-0.04}$	1591/1594	$\geq 193$ $158^{+8}_{-7}$	C. Ricci et al. (2017) J. T. Hinkle & R. Mushotzky (2021)
3C 206	$1.76^{+0.05}_{-0.05}$	$112^{+47}_{-33}$	$<0.59$	272/264	$\geq 272$ $>68$ $>53$ $>79$	C. Ricci et al. (2017) J. Kang et al. (2020) N. Kamraj et al. (2022) A. Akylas & I. Georgantopoulos (2021)
3C 227	$1.79^{+0.05}_{-0.04}$	$>152$	$<0.24$	264/290	$\geq 90$ $>87$	C. Ricci et al. (2017) J. Kang et al. (2020)
3C 380	$1.66^{+0.06}_{-0.06}$	$>217$	$<0.28$	198/178	...	...
3C 382	$1.65^{+0.01}_{-0.01}$	$111^{+22}_{-19}$	$0.13^{+0.03}_{-0.03}$	1188/1244	$158^{+39}_{-76}$ $133^{+98}_{-40}$ $215^{+150}_{-60}$	N. Kamraj et al. (2022) S. H. Ezhikode et al. (2020) A. Tortosa et al. (2018)
3C 390.3	$1.77^{+0.01}_{-0.01}$	$144^{+34}_{-19}$	$0.21^{+0.07}_{-0.08}$	997/1017	$166^{+64}_{-57}$ $130^{+42}_{-32}$ $120 \pm 20$	C. Ricci et al. (2017) M. Molina et al. (2019) A. Tortosa et al. (2018)
6dF J1254564-265702	$1.58^{+0.04}_{-0.05}$	$32^{+7}_{-5}$	$<0.78$	164/186	$\geq 42$ $91^{+100}_{-50}$	C. Ricci et al. (2017) A. Akylas & I. Georgantopoulos (2021)
ARK 120	$1.95^{+0.03}_{-0.03}$	$346^{+422}_{-133}$	$0.51^{+0.10}_{-0.09}$	1147/1146	$\geq 292$ $>763$ $233^{+147}_{-67}$	C. Ricci et al. (2017) N. Kamraj et al. (2022) A. Akylas & I. Georgantopoulos (2021)
Ark 241	$1.88^{+0.05}_{-0.05}$	$>115$	$0.90^{+0.60}_{-0.47}$	197/214	...	...
ARK 564	$2.41^{+0.04}_{-0.03}$	$73^{+30}_{-16}$	$0.34^{+0.12}_{-0.07}$	582/574	$43^{+3}_{-3}$	E. Kara et al. (2017)
CGCG 229-015	$1.71^{+0.08}_{-0.06}$	$46^{+14}_{-8}$	$0.93^{+0.74}_{-0.56}$	164/173	$\geq 38$ $54^{+76}_{-22}$	C. Ricci et al. (2017) A. Akylas & I. Georgantopoulos (2021)
ESO 025-G002	$1.67^{+0.04}_{-0.04}$	$133^{+93}_{-26}$	$>0.23$	385/417	$\geq 23$	C. Ricci et al. (2017)
ESO 031-G008	$2.04^{+0.04}_{-0.04}$	$>286$	$0.74^{+0.37}_{-0.29}$	305/354	$\geq 76$	C. Ricci et al. (2017)
ESO 209-12	$1.90^{+0.04}_{-0.03}$	$>260$	$0.38^{+0.24}_{-0.22}$	399/427	$\geq 91$	C. Ricci et al. (2017)
ESO 323-G077	$1.45^{+0.03}_{-0.03}$	$89^{+14}_{-13}$	$2.40^{+0.85}_{-0.57}$	409/386	$115^{+114}_{-42}$	N. Kamraj et al. (2022)
ESO 416-G002	$1.81^{+0.07}_{-0.07}$	$>172$	$0.31^{+0.47}_{-0.23}$	119/125	$\geq 366$	C. Ricci et al. (2017)
ESO 511-G030	$1.70^{+0.04}_{-0.04}$	$69^{+29}_{-15}$	$0.80^{+0.50}_{-0.41}$	308/289	$\geq 591$	C. Ricci et al. (2017)
ESO381-G007	$1.66^{+0.07}_{-0.07}$	$64^{+35}_{-18}$	$<1.00$	163/161	$\geq 76$	C. Ricci et al. (2017)

**Table 3**  
(Continued)

Source	$\Gamma$	$E_{\text{cut}}$ (keV)	$R$	$\chi^2/\text{dof}$	$E_{\text{cut}}$ from the Literature	References
FAIRALL 1146	$2.03^{+0.03}_{-0.03}$	$138^{+73}_{-39}$	$1.12^{+0.42}_{-0.35}$	433/423	$\geq 72$	C. Ricci et al. (2017)
Fairall 51	$1.53^{+0.33}_{-0.09}$	$62^{+115}_{-14}$	$4.11^{+1.49}_{-0.62}$	780/762	$> 166$	N. Kamraj et al. (2022)
GRS 1734-292	$1.67^{+0.02}_{-0.01}$	$75^{+6}_{-5}$	$0.27^{+0.11}_{-0.06}$	894/923	$\geq 105$	C. Ricci et al. (2017)
					$84^{+38}_{-26}$	C. Ricci et al. (2017)
					$53^{+13}_{-9}$	M. Molina et al. (2019)
H1821+643	$1.91^{+0.03}_{-0.03}$	$229^{+221}_{-77}$	$0.23^{+0.21}_{-0.19}$	450/454	$53 \pm 10$	A. Tortosa et al. (2018)
					$\geq 130$	C. Ricci et al. (2017)
HE 1143–1810	$1.79^{+0.07}_{-0.06}$	$104^{+24}_{-17}$	$0.33^{+0.15}_{-0.14}$	524/617	$114^{+159}_{-44}$	A. Akylas & I. Georgantopoulos (2021)
HE 1136–2304	$1.61^{+0.02}_{-0.02}$	$80^{+15}_{-11}$	$0.18^{+0.14}_{-0.12}$	648/650	$183^{+319}_{-59}$	C. Ricci et al. (2017)
					$\geq 63$	C. Ricci et al. (2017)
IC 1198	$1.75^{+0.06}_{-0.05}$	$124^{+107}_{-43}$	$0.96^{+0.68}_{-0.47}$	191/195	$97^{+136}_{-77}$	Y. Diaz et al. (2023)
IC 4329A	$1.77^{+0.01}_{-0.01}$	$191^{+14}_{-10}$	$0.32^{+0.04}_{-0.02}$	2211/2088	...	...
IGR J14471-6414	$2.01^{+0.08}_{-0.08}$	$> 153$	$< 1.98$	115/106	$236^{+42}_{-26}$	C. Ricci et al. (2017)
IGRJ14552–5133	$1.93^{+0.02}_{-0.02}$	$254^{+194}_{-72}$	$0.55^{+0.15}_{-0.15}$	741/775	$\geq 78$	C. Ricci et al. (2017)
IGR J19378-0617	$2.11^{+0.07}_{-0.06}$	$228^{+419}_{-83}$	$0.75^{+0.35}_{-0.20}$	757/786	$\geq 59$	C. Ricci et al. (2017)
					$\geq 126$	C. Ricci et al. (2017)
					$241^{+1377}_{-114}$	N. Kamraj et al. (2022)
IRAS 05589+2828	$1.83^{+0.11}_{-0.09}$	$136^{+109}_{-56}$	$1.25^{+0.57}_{-0.36}$	843/771	$71^{+20}_{-14}$	C. Ricci et al. (2017)
IRAS 09149-6206	$1.69^{+0.14}_{-0.19}$	$81^{+60}_{-26}$	$0.80^{+0.13}_{-0.11}$	1000/1005	$\geq 99$	C. Ricci et al. (2017)
IRAS F12397+3333	$2.34^{+0.04}_{-0.04}$	$> 97$	$0.76^{+0.38}_{-0.36}$	453/399	...	...
IRAS 04124–0803	$1.53^{+0.04}_{-0.04}$	$80^{+21}_{-14}$	$0.52^{+0.27}_{-0.25}$	298/330	$\geq 40$	C. Ricci et al. (2017)
IRAS04392-2713	$1.92^{+0.06}_{-0.06}$	$> 188$	$0.46^{+0.20}_{-0.28}$	172/185	$\geq 43$	C. Ricci et al. (2017)
KUG 1141+371	$1.92^{+0.11}_{-0.14}$	$90^{+27}_{-17}$	$0.39^{+0.22}_{-0.19}$	470/514	...	...
MCG-06-30-15	$1.82^{+0.11}_{-0.09}$	$126^{+23}_{-19}$	$0.98^{+0.66}_{-0.34}$	1574/1516	$123^{+101}_{-39}$	C. Ricci et al. (2017)
					$170^{+240}_{-53}$	M. Dadina (2007)
					$63^{+24}_{-14}$	A. Malizia et al. (2014)
					$> 110$	A. Tortosa et al. (2018)
MCG+05-40-026	$1.77^{+0.07}_{-0.06}$	$104^{+151}_{-41}$	$< 0.96$	161/155	...	...
MCG+08-11-011	$1.83^{+0.01}_{-0.01}$	$153^{+15}_{-13}$	$0.40^{+0.06}_{-0.05}$	1506/1419	$252^{+131}_{-60}$	C. Ricci et al. (2017)
					$163^{+53}_{-32}$	M. Molina et al. (2019)
					$171^{+44}_{-30}$	A. Malizia et al. (2014)
					$175^{+110}_{-50}$	A. Tortosa et al. (2018)
MR 2251–178	$1.63^{+0.01}_{-0.02}$	$96^{+17}_{-9}$	$< 0.06$	818/859	$\geq 59$	C. Ricci et al. (2017)
					$132^{+130}_{-68}$	M. Dadina (2007)
					$138^{+57}_{-38}$	A. Malizia et al. (2014)
MRK 1040	$1.88^{+0.01}_{-0.01}$	$300^{+108}_{-70}$	$0.61^{+0.11}_{-0.10}$	1025/1007	$\geq 152$	C. Ricci et al. (2017)
					$> 356$	S. H. Ezhikode et al. (2020)
					$198^{+212}_{-70}$	N. Kamraj et al. (2022)
MRK 1044	$1.80^{+0.05}_{-0.06}$	$381^{+553}_{-179}$	$0.50^{+0.14}_{-0.11}$	1004/1004	$\geq 99$	C. Ricci et al. (2017)
					$> 120$	A. Akylas & I. Georgantopoulos (2021)
					$\geq 214$	N. Kamraj et al. (2018)
MRK 110	$1.70^{+0.01}_{-0.01}$	$92^{+12}_{-10}$	$0.12^{+0.02}_{-0.02}$	1624/1576	$191^{+207}_{-57}$	C. Ricci et al. (2017)
					$117^{+12}_{-17}$	D. Porquet et al. (2021)
MRK 1148	$1.76^{+0.03}_{-0.03}$	$99^{+30}_{-20}$	$< 0.22$	545/532	$\geq 71$	C. Ricci et al. (2017)
					$101^{+11}_{-9}$	J. T. Hinkle & R. Mushotzky (2021)
MRK 1310	$1.82^{+0.04}_{-0.04}$	$> 173$	$0.28^{+0.31}_{-0.22}$	304/293	$\geq 62$	C. Ricci et al. (2017)
MRK 1383	$1.92^{+0.02}_{-0.02}$	$> 276$	$0.98^{+0.21}_{-0.21}$	818/768	...	...
MRK 1392	$1.93^{+0.06}_{-0.05}$	$> 187$	$0.84^{+0.50}_{-0.45}$	185/193	$\geq 91$	C. Ricci et al. (2017)
MRK 1393	$1.95^{+0.04}_{-0.04}$	$> 295$	$0.37^{+0.26}_{-0.21}$	352/376	$\geq 140$	C. Ricci et al. (2017)
MRK 205	$1.92^{+0.05}_{-0.05}$	$131^{+122}_{-45}$	$0.60^{+0.44}_{-0.35}$	259/255	$\geq 56$	C. Ricci et al. (2017)
					$> 108$	A. Akylas & I. Georgantopoulos (2021)
					$> 365$	N. Kamraj et al. (2018)
MRK 279	$1.49^{+0.04}_{-0.05}$	$68^{+18}_{-13}$	$0.18^{+0.11}_{-0.12}$	989/994	$\geq 125$	C. Ricci et al. (2017)
MRK 290	$1.59^{+0.04}_{-0.04}$	$102^{+46}_{-25}$	$0.33^{+0.28}_{-0.22}$	316/364	$184^{+256}_{-100}$	C. Ricci et al. (2017)
					$> 53$	S. H. Ezhikode et al. (2020)
MRK 335	$1.98^{+0.26}_{-0.18}$	$> 74$	$4.52^{+3.73}_{-1.10}$	764/771	$\geq 185$	C. Ricci et al. (2017)
MRK 359	$1.91^{+0.03}_{-0.03}$	$> 163$	$0.86^{+0.35}_{-0.31}$	485/433	$\geq 40$	C. Ricci et al. (2017)
Mrk 509	$1.77^{+0.02}_{-0.03}$	$123^{+17}_{-18}$	$0.32^{+0.07}_{-0.07}$	1673/1603	$102^{+43}_{-19}$	C. Ricci et al. (2017)
					$60^{+71}_{-23}$	M. Dadina (2007)

**Table 3**  
(Continued)

Source	$\Gamma$	$E_{\text{cut}}$ (keV)	$R$	$\chi^2/\text{dof}$	$E_{\text{cut}}$ from the Literature	References
MRK 590	$1.68^{+0.02}_{-0.02}$	$127^{+33}_{-23}$	$0.23^{+0.13}_{-0.11}$	818/775	$\geq 112$ $66^{+86}_{-26}$	C. Ricci et al. (2017) A. Akylas & I. Georgantopoulos (2021)
MRK 595	$1.31^{+0.18}_{-0.23}$	>35	frozen	104/100	$75^{+408}_{-42}$	C. Ricci et al. (2017)
MRK 684	$2.14^{+0.09}_{-0.08}$	>150	<2.52	99/103	$\geq 127$	C. Ricci et al. (2017)
MRK 704	$1.80^{+0.04}_{-0.04}$	$207^{+146}_{-64}$	$1.11^{+0.48}_{-0.32}$	374/342	$\geq 261$	C. Ricci et al. (2017)
MRK 732	$1.78^{+0.04}_{-0.04}$	>279	$0.20^{+0.27}_{-0.18}$	324/352	$81^{+200}_{-40}$	C. Ricci et al. (2017)
MRK 79	$1.86^{+0.05}_{-0.05}$	$349^{+516}_{-152}$	$0.55^{+0.18}_{-0.15}$	993/968	$224^{+366}_{-97}$ $402^{+165}_{-90}$	C. Ricci et al. (2017) N. Kamraj et al. (2022)
MRK 813	$1.98^{+0.04}_{-0.04}$	>252	$0.49^{+0.35}_{-0.24}$	345/321	$\geq 60$	C. Ricci et al. (2017)
MRK 817	$1.65^{+0.29}_{-0.18}$	>68	$1.64^{+0.39}_{-0.32}$	1013/1007	$\geq 242$	C. Ricci et al. (2017)
MRK 841	$1.80^{+0.03}_{-0.03}$	$125^{+49}_{-30}$	$0.42^{+0.23}_{-0.19}$	467/508	$\geq 152$ $139^{+142}_{-49}$	C. Ricci et al. (2017) J. T. Hinkle & R. Mushotzky (2021)
MRK 876	$1.81^{+0.06}_{-0.06}$	$140^{+154}_{-52}$	$0.74^{+0.55}_{-0.40}$	193/187	$\geq 43$	C. Ricci et al. (2017)
MRK 885	$1.90^{+0.08}_{-0.06}$	>161	$0.56^{+0.83}_{-0.30}$	172/151	$\geq 212$	C. Ricci et al. (2017)
MRK 915	$1.72^{+0.03}_{-0.03}$	$136^{+68}_{-36}$	$0.42^{+0.26}_{-0.22}$	519/547	$\geq 79$ $58^{+11}_{-7}$	C. Ricci et al. (2017) J. T. Hinkle & R. Mushotzky (2021)
MRK 926	$1.70^{+0.02}_{-0.01}$	$142^{+33}_{-19}$	$0.11^{+0.03}_{-0.02}$	1491/1493	$320^{+166}_{-79}$ $211^{+235}_{-95}$	C. Ricci et al. (2017) M. Dadina (2007)
Mrk739E	$2.07^{+0.07}_{-0.07}$	>241	$0.84^{+0.43}_{-0.48}$	133/132	$\geq 50$	C. Ricci et al. (2017)
NGC 0985	$1.84^{+0.03}_{-0.03}$	>188	$0.42^{+0.21}_{-0.25}$	393/469	$\geq 102$	C. Ricci et al. (2017)
NGC 3227	$1.64^{+0.01}_{-0.01}$	$94^{+7}_{-6}$	$0.62^{+0.10}_{-0.10}$	1224/1163	$94^{+16}_{-12}$ $60^{+5}_{-4}$	C. Ricci et al. (2017) J. T. Hinkle & R. Mushotzky (2021)
NGC 3516	$1.90^{+0.03}_{-0.03}$	>448	$1.27^{+0.29}_{-0.14}$	696/655	$87^{+16}_{-12}$ $132^{+87}_{-43}$	N. Kamraj et al. (2022) C. Ricci et al. (2017)
NGC 3783	$1.55^{+0.07}_{-0.03}$	$112^{+24}_{-19}$	$0.90^{+0.11}_{-0.12}$	1137/1145	$77^{+16}_{-11}$ $98^{+79}_{-34}$	N. Kamraj et al. (2022) A. C. Fabian et al. (2015)
NGC 4051	$1.78^{+0.07}_{-0.07}$	>452	$1.33^{+1.02}_{-0.67}$	1674/1647	$59^{+25}_{-13}$	C. Ricci et al. (2017)
NGC 4579	$1.73^{+0.06}_{-0.06}$	$82^{+49}_{-23}$	$0.29^{+0.09}_{-0.07}$	819/739	...	...
NGC 4593	$1.87^{+0.02}_{-0.02}$	>648	$0.57^{+0.26}_{-0.13}$	523/571	$\geq 655$	C. Ricci et al. (2017)
NGC 5273	$1.46^{+0.06}_{-0.06}$	$68^{+25}_{-16}$	$1.03^{+0.33}_{-0.28}$	593/574	$\geq 294$ $115^{+91}_{-37}$	C. Ricci et al. (2017) A. Akylas & I. Georgantopoulos (2021)
NGC 5548	$1.71^{+0.03}_{-0.01}$	$118^{+12}_{-8}$	$0.48^{+0.10}_{-0.06}$	1219/1143	$\geq 220$ $\geq 281$	N. Kamraj et al. (2022) C. Ricci et al. (2017)
NGC 7469	$1.95^{+0.02}_{-0.02}$	$122^{+27}_{-21}$	$0.77^{+0.19}_{-0.18}$	647/692	$\geq 316$ $70^{+40}_{-10}$ $113^{+33}_{-32}$	C. Ricci et al. (2017) J. T. Hinkle & R. Mushotzky (2021)
NGC 931	$1.88^{+0.01}_{-0.01}$	$229^{+78}_{-42}$	$0.63^{+0.12}_{-0.12}$	974/954	$\geq 152$	C. Ricci et al. (2017)
PG 0026+129	$1.82^{+0.02}_{-0.02}$	$110^{+20}_{-15}$	$0.34^{+0.12}_{-0.11}$	903/856	$\geq 45$	C. Ricci et al. (2017)
PG 0052+251	$1.66^{+0.02}_{-0.01}$	>76	<0.18	167/190	$\geq 137$	C. Ricci et al. (2017)
PG 0804+761	$1.94^{+0.05}_{-0.05}$	>269	$0.71^{+0.49}_{-0.35}$	217/221	$\geq 67$	C. Ricci et al. (2017)
RBS 1037	$2.00^{+0.06}_{-0.06}$	>133	$1.04^{+0.28}_{-0.30}$	208/200	$\geq 34$	C. Ricci et al. (2017)
RBS 0295	$1.73^{+0.06}_{-0.05}$	>91	<0.42	212/218	...	...
RBS 0770	$1.65^{+0.07}_{-0.04}$	$59^{+18}_{-12}$	$0.57^{+0.22}_{-0.18}$	755/713	$\geq 256$ $\geq 267$	C. Ricci et al. (2017) N. Kamraj et al. (2018)
S52116+81	$1.75^{+0.04}_{-0.04}$	$103^{+40}_{-24}$	$0.37^{+0.27}_{-0.22}$	370/409	$\geq 175$ $\geq 93$	C. Ricci et al. (2017) M. Molina et al. (2019)
SDSS J114921.52+532013.4	$1.53^{+0.10}_{-0.10}$	$29^{+9}_{-7}$	<2.02	88/75	$47^{+86}_{-14}$	C. Ricci et al. (2017)
SDSS J104326.47+110524.2	$1.72^{+0.05}_{-0.05}$	>123	<0.43	220/236	$\geq 91$	C. Ricci et al. (2017)
SWIFT J2127.4+5654	$1.89^{+0.01}_{-0.01}$	$84^{+6}_{-6}$	$0.75^{+0.10}_{-0.09}$	1094/1089	$62^{+25}_{-15}$ $92^{+26}_{-17}$	C. Ricci et al. (2017) J.-L. Kang et al. (2021)
UGC 10120	$1.91^{+0.07}_{-0.06}$	>225	<0.71	185/192	...	...
UGC 3478	$1.99^{+0.06}_{-0.06}$	>98	<1.07	212/196	...	...
UGC 03601	$1.49^{+0.09}_{-0.08}$	$58^{+45}_{-19}$	<0.86	127/109	$74^{+240}_{-32}$	C. Ricci et al. (2017)
UGC 06728	$1.62^{+0.05}_{-0.05}$	$66^{+20}_{-14}$	$0.55^{+0.43}_{-0.32}$	223/241	$73^{+31}_{-19}$ $63^{+133}_{-25}$	C. Ricci et al. (2017) N. Kamraj et al. (2022)
VII ZW 653	$2.05^{+0.05}_{-0.05}$	>114	$1.10^{+0.61}_{-0.51}$	187/213	...	...
VII ZW 742	$1.88^{+0.08}_{-0.08}$	>174	$1.25^{+1.04}_{-0.71}$	99/108	$\geq 52$	C. Ricci et al. (2017)



**Table 4**  
(Continued)

Source	$N_{\text{H}}^{\text{INT}}$ ( $10^{22}$ atoms $\text{cm}^{-2}$ )	$\Gamma$	$kT_e$ (keV)	$R$	$N_{\text{relxillCP}}$ ( $10^{-4}$ photons $\text{keV}^{-1} \text{cm}^{-2} \text{s}^{-1}$ )	$N_{\text{xillverCP}}$ ( $10^{-4}$ photons $\text{keV}^{-1} \text{cm}^{-2} \text{s}^{-1}$ )	$\chi^2/\text{dof}$
MRK 205	...	$1.97^{+0.04}_{-0.04}$	$>20$	$0.57^{+0.43}_{-0.35}$	...	$0.47^{+0.02}_{-0.02}$	260/255
MRK 279	...	$1.68^{+0.01}_{-0.01}$	$15^{+2}_{-2}$	$0.13^{+0.09}_{-0.08}$	$0.29^{+0.02}_{-0.01}$	$0.09^{+0.02}_{-0.02}$	1007/995
MRK 290	...	$1.70^{+0.03}_{-0.03}$	$>15$	$<0.51$	...	$0.43^{+0.01}_{-0.01}$	319/364
Mrk 509	...	$1.82^{+0.02}_{-0.01}$	$23^{+3}_{-2}$	$0.19^{+0.03}_{-0.04}$	$2.15^{+0.05}_{-0.04}$	...	1691/1603
MRK 590	$2.07^{+0.59}_{-0.57}$	$1.82^{+0.03}_{-0.03}$	$>49$	$0.20^{+0.12}_{-0.11}$	$0.92^{+0.19}_{-0.16}$	...	815/774
MRK 704	$10.24^{+1.38}_{-1.36}$	$1.86^{+0.03}_{-0.03}$	$>30$	$1.11^{+0.50}_{-0.37}$	...	$0.62^{+0.04}_{-0.03}$	374/342
MRK 79	...	$1.88^{+0.04}_{-0.04}$	$>47$	$0.53^{+0.19}_{-0.16}$	$1.26^{+0.06}_{-0.13}$	...	994/968
MRK 841	...	$1.86^{+0.02}_{-0.02}$	$33^{+185}_{-14}$	$0.37^{+0.23}_{-0.19}$	...	$0.89^{+0.02}_{-0.02}$	469/508
MRK 876	...	$1.86^{+0.05}_{-0.04}$	$>15$	$0.70^{+0.56}_{-0.39}$	...	$0.18^{+0.01}_{-0.01}$	192/187
MRK 915	$6.90^{+0.98}_{-1.04}$	$1.81^{+0.03}_{-0.03}$	$>28$	$0.33^{+0.25}_{-0.16}$	...	$0.45^{+0.01}_{-0.02}$	522/547
MRK 926	...	$1.78^{+0.01}_{-0.01}$	$31^{+7}_{-5}$	$0.10^{+0.02}_{-0.02}$	$3.13^{+0.11}_{-0.09}$	...	1525/1494
NGC 3227	$2.66^{+0.34}_{-0.33}$	$1.76^{+0.01}_{-0.01}$	$26^{+6}_{-4}$	$0.56^{+0.09}_{-0.09}$	...	$1.89^{+0.02}_{-0.02}$	1198/1163
NGC 3783	...	$1.74^{+0.02}_{-0.02}$	$48^{+48}_{-9}$	$0.41^{+0.20}_{-0.16}$	$2.33^{+0.23}_{-0.15}$	$0.76^{+0.27}_{-0.26}$	1270/1132
NGC 4579	...	$1.84^{+0.03}_{-0.03}$	$23^{+23}_{-7}$	$0.25^{+0.09}_{-0.07}$	$0.35^{+0.04}_{-0.03}$	...	828/739
NGC 5273	...	$1.79^{+0.06}_{-0.10}$	$>18$	$0.98^{+0.53}_{-0.33}$	$1.00^{+0.21}_{-0.20}$	...	589/572
NGC 5548	$3.32^{+0.34}_{-0.35}$	$1.81^{+0.01}_{-0.01}$	$35^{+9}_{-7}$	$0.43^{+0.10}_{-0.09}$	...	$2.23^{+0.07}_{-0.03}$	1228/1143
NGC 7469	...	$2.00^{+0.02}_{-0.02}$	$45^{+52}_{-17}$	$0.74^{+0.20}_{-0.17}$	...	$1.59^{+0.03}_{-0.03}$	650/692
NGC 931	...	$1.91^{+0.01}_{-0.01}$	$>50$	$0.58^{+0.14}_{-0.09}$	...	$1.40^{+0.02}_{-0.02}$	979/954
PG 0026+129	...	$1.89^{+0.01}_{-0.01}$	$22^{+9}_{-4}$	$0.30^{+0.12}_{-0.11}$	...	$0.39^{+0.12}_{-0.11}$	899/856
RBS 0770	...	$1.78^{+0.02}_{-0.02}$	$15^{+3}_{-2}$	$0.42^{+0.16}_{-0.13}$	$0.75^{+0.04}_{-0.04}$	...	757/713
S52116+81	...	$1.84^{+0.03}_{-0.03}$	$>18$	$0.29^{+0.26}_{-0.20}$	...	$0.74^{+0.02}_{-0.02}$	373/409
SDSS J114921.52 +532013.4	...	$1.76^{+0.07}_{-0.07}$	$7^{+1}_{-1}$	$1.38^{+3.34}_{-1.26}$	...	$0.08^{+0.01}_{-0.01}$	88/75
SWIFT J2127.4+5654	...	$1.96^{+0.01}_{-0.01}$	$21^{+3}_{-2}$	$0.72^{+0.10}_{-0.10}$	...	$1.49^{+0.01}_{-0.01}$	1084/1089
UGC 03601	...	$1.68^{+0.07}_{-0.06}$	$>9$	$<0.53$	...	$0.24^{+0.01}_{-0.01}$	129/109
UGC 06728	...	$1.73^{+0.07}_{-0.07}$	$17^{+25}_{-5}$	$0.34^{+0.42}_{-0.21}$	$0.31^{+0.58}_{-0.39}$	...	223/239

**Appendix B** **$kT_e$ : The Temperature of the Corona**

Here, we discuss the results obtained from the spectral analysis using the model  $\text{CONST} \times \text{TBABS} \times \text{ZTBABS} \times (\text{XILLVERCP}/\text{RELXILLCP}/(\text{RELXILLCP}+\text{XILLVERCP}))$ . We also compare the best-fit values of our analysis with the previously measured values of  $kT_e$  from the literature, if available. Among the 42 sources for which we could constrain  $kT_e$ , 18 sources were already discussed by us earlier (I. Pal et al. 2022; I. Pal & C. S. Stalin 2023). Therefore, here we give details on the rest of the 24 sources.

**2MASX J23013626-5913210.** This source at a redshift  $z = 0.150$  was observed by NuSTAR once in 2017. We used Model 2a to estimate the coronal properties of the source. We found the source spectra to be well described with  $\Gamma = 1.87^{+0.04}_{-0.04}$  and  $kT_e = 13.35^{+0.6,23}_{-0.3,48}$  keV. Previously, using a similar Comptonization model, N. Kamraj et al. (2022) found a value of  $\Gamma = 1.78^{+0.14}_{-0.11}$  and  $kT_e = 11.10^{+12.22}_{-02.87}$  keV. Our results are thus in agreement with N. Kamraj et al. (2022).

**3C 120.** This is a radio-loud Seyfert 1 galaxy at  $z = 0.033$ . NuSTAR observed the source twice on the same day in February 2013. Of the two observations, we analyzed the spectrum with the highest exposure time using Model 2b. We obtained values of  $\Gamma = 1.85^{+0.01}_{-0.01}$  and  $kT_e = 45.31^{+18.79}_{-07.82}$  keV. Analyzing the same data set using RELXILLCP, J.-L. Kang & J.-X. Wang (2022) found a lower limit of  $kT_e > 91$  keV.

**3C 390.3.** This radio-loud Seyfert 1 galaxy at  $z = 0.05613$  was observed twice by NuSTAR on the same day in 2013 May.

From spectral analysis of the data using Model 2a, we obtained  $\Gamma = 1.84^{+0.01}_{-0.01}$  and  $kT_e = 44.13^{+54.75}_{-12.50}$  keV. For the same data set, J.-L. Kang & J.-X. Wang (2022) and N. Kamraj et al. (2022) reported lower limits of  $kT_e > 46$  keV and  $kT_e > 49.86$  keV, respectively.

**ARK 564.** This source was observed by NuSTAR three times between 2015 May and 2018 November. Of these, results of the observation done by NuSTAR in 2018 September are reported in this work for the first time. Fitting the observed data with Model 2c, we obtained  $\Gamma = 2.40^{+0.02}_{-0.02}$  and  $kT_e = 24.28^{+13.60}_{-04.29}$  keV, respectively. From analysis of the data acquired by NuSTAR in 2015, E. Kara et al. (2017) determined  $kT_e = 15 \pm 2$  keV, arguing that the source has the coolest corona. Also, based on two epochs of data, S. Barua et al. (2020) reported variation in the temperature of the corona.

**HE 1136-2304.** AGN exhibit flux variations across various timescales and across the entire electromagnetic spectrum. In the last decade, an increasing number of sources have displayed notably more pronounced changes in their flux and spectral characteristics, both in the X-ray range and the optical/UV range. These events are often referred to as changing-look AGN (C. Ricci & B. Trakhtenbrot 2023). HE 1136-2304 is such a changing-look AGN. It was found to change its optical spectral nature from Type 2 in 1993 to Type 1.5 in 2014 (M. L. Parker et al. 2016). It was observed by NuSTAR twice on the same day in 2014 July. Of the two, we analyzed the spectrum with the maximum exposure. The best-fit values obtained from fitting Model 2a to the source spectrum were

$\Gamma = 1.78^{+0.03}_{-0.02}$  and  $kT_e = 27.81^{+78.85}_{-09.30}$  keV. From an analysis of the same NuSTAR spectrum using RELXILLCP, J.-L. Kang & J.-X. Wang (2022) obtained a lower limit of  $kT_e > 21$  keV.

*IC 4329A*. This Seyfert 1 galaxy was observed six times by NuSTAR, once in 2012 and the others during 2021 August. We analyzed here the NuSTAR spectrum taken in 2012. Fitting the spectrum using Model 2a, we obtained best-fit values of  $\Gamma$  and  $kT_e$  as  $1.83^{+0.003}_{-0.003}$  and  $64.16^{+15.41}_{-11.63}$  keV, respectively. This source has been studied extensively in the past. For example, A. Tortosa et al. (2018) reported  $kT_e = 37 \pm 7$  keV from fitting COMPTT for a slab geometry. J.-L. Kang & J.-X. Wang (2022) estimated  $kT_e = 71^{+37}_{-15}$  keV using the RELXILLCP model. N. Kamraj et al. (2022) also found  $kT_e = 82^{+16}_{-7}$  keV from an XILLVERCP fit to the source spectrum.

*2MASX J21355399+4728217*. This Seyfert galaxy was observed by NuSTAR in 2019 September. From the analysis of the source spectrum, A. Akylas & I. Georgantopoulos (2021) reported  $E_{\text{cut}} = 55^{+50}_{-19}$  keV. We analyzed the same observation ID using Model 2a and found  $kT_e = 15.57^{+12.24}_{-03.90}$  keV.

*IRAS 04124-0803*. Analysis of the NuSTAR observations (done in 2021 September) on this source is carried out for the first time. From fitting Model 2a to the source spectrum, we obtained best-fit values of  $\Gamma = 1.66^{+0.03}_{-0.03}$  and  $kT_e = 14.88^{+03.70}_{-02.57}$  keV.

*IRAS 09149-6206*. Results on NuSTAR observations of this source are reported for the first time. This source was observed by NuSTAR twice between 2018 July and August. We modeled the Comptonized spectrum (observed in 2018 August) and estimated the best-fit value of  $kT_e$  using Model 2b. From the model fit to the spectrum, we obtained  $\Gamma = 1.90^{+0.11}_{-0.09}$  and  $kT_e = 18.09^{+16.87}_{-04.07}$  keV.

*IRAS 05589+2828*. This Seyfert 1 galaxy situated at  $z = 0.02940$  was observed by NuSTAR in 2020 April. The temperature of the corona of the source is reported for the first time. From the physical model fit to the observed spectrum, we found values of  $\Gamma = 1.90^{+0.11}_{-0.07}$  and  $kT_e = 42.90^{+120.46}_{-23.92}$  keV.

*Mrk 1148*. This Seyfert 1 galaxy was observed by NuSTAR in 2018 January. We carried out the spectral analysis using Model 2a. The best-fit values obtained using the model fit to the spectrum are  $\Gamma = 1.86^{+0.02}_{-0.02}$  and  $kT_e = 24.04^{+19.81}_{-06.76}$  keV. Recently, analyzing the same spectrum, both N. Kamraj et al. (2022) and J.-L. Kang & J.-X. Wang (2022) found values of  $kT_e > 18$  keV.

*Mrk 509*. NuSTAR observed this source two times between 2015 April and June. In this work, we analyzed the spectrum taken in 2015 April. From fitting Model 2c to the observed spectrum, we obtained  $\Gamma = 1.86^{+0.01}_{-0.02}$  and  $kT_e = 35.78^{+06.78}_{-05.72}$  keV. On analysis of the same spectrum using the RELXILLCP model J.-L. Kang & J.-X. Wang (2022) reported  $kT_e = 24 \pm 2$  keV.

*2MASX J18560128+1538059*. This Seyfert 1 galaxy was observed by NuSTAR in 2017, and from the analysis of the source spectrum using our Model 2a, we found  $kT_e = 12.32^{+3.12}_{-2.36}$  keV. Using the same observation ID, A. Akylas & I. Georgantopoulos (2021) reported  $E_{\text{cut}} = 43^{+20}_{-11}$  keV.

*PG 0026+129*. NuSTAR observed the Seyfert 1 galaxy once in 2021 January and the results of the analysis of the observation are reported for the first time. From the Model 2a fit to the observed spectrum, we obtained best-fit values of  $\Gamma = 1.89^{+0.01}_{-0.01}$  and  $kT_e = 22.18^{+08.88}_{-04.03}$  keV.

*SWIFT J2127.4+5654*. This source, classified as a narrow-line Seyfert 1 galaxy, was observed by NuSTAR nine times between 2012 September and 2018 December. We analyzed the observations carried out by NuSTAR in 2012 September, as

it has the maximum exposure time. By fitting the observed spectrum using Model 2a, we obtained  $\Gamma = 1.96^{+0.01}_{-0.01}$  and  $kT_e = 20.70^{+03.36}_{-01.94}$  keV. From an analysis of the same spectrum, J.-L. Kang et al. (2021) reported a  $kT_e$  of  $21^{+2}_{-2}$  keV.

*IGR J19378-0617*. This source is situated at  $z = 0.0103$ . It was classified as a Seyfert 1 galaxy, observed six times by NuSTAR between 2015 and 2022. From fitting the source spectrum using Model 2a, we found  $kT_e = 49.35^{+36.94}_{-13.04}$  keV. From the spectral analysis of the source spectrum, N. Kamraj et al. (2022) reported  $kT_e > 122$  keV.

*Fairall 51*. NuSTAR observed this Seyfert 1 galaxy four times between 2018 and 2021. We analyzed the NuSTAR spectrum observed in 2018 June. From fitting the source spectrum using Model 2a, we found  $kT_e = 19.48^{+6.54}_{-1.83}$  keV.

*Mrk 279*. This Seyfert 1 galaxy was observed four times by NuSTAR between 2019 and 2020. We analyzed the 2020 August spectrum using Model 2c and found  $kT_e = 16.38^{+1.72}_{-1.55}$  keV. By analyzing the source spectrum taken in 2019 October, J.-L. Kang & J.-X. Wang (2022) reported a lower limit of  $kT_e > 84$  keV.

*ESO 323-G077*. This source is classified as a Seyfert 1.5 galaxy (H. Winkler 1992), situated at  $z = 0.0155$ . NuSTAR observed this source six times between 2016 August and 2017 February. We analyzed 2017 January NuSTAR data. From the Model 2a fit to the source spectrum, we obtained  $kT_e = 35.21^{+13.02}_{-11.89}$  keV, this value is also consistent with R. Serafinelli et al. (2023). For this source, N. Kamraj et al. (2022) reported a lower limit of  $kT_e > 34$  keV.

*3C 109*. This Seyfert galaxy was observed by NuSTAR twice in 2017 August. We analyzed the one with the maximum exposure time. By fitting Model 2a to the source spectrum, we found  $kT_e = 18.09^{+6.91}_{-2.72}$  keV.




*RBS 0770*. This source was observed four times between 2012 and 2021 by NuSTAR. By fitting Model 2a to the source spectrum, we found  $kT_e = 17.71^{+4.30}_{-2.38}$  keV. From the analysis of the same observation, N. Kamraj et al. (2022) reported a lower limit for  $kT_e > 24$  keV.

*CGCG 229-015*. This nearby Seyfert 1 galaxy was observed once by NuSTAR in 2018 February. From an analysis of the same observation ID, A. Akylas & I. Georgantopoulos (2021) reported  $E_{\text{cut}} = 54^{+13.02}_{-11.89}$  keV. From the Model 2a fit to the source spectrum, we obtained  $kT_e = 17.00^{+41.62}_{-5.61}$  keV.

*3C 382*. This Seyfert galaxy was observed seven times between 2012 and 2016. We analyzed the 2013 spectrum and reported  $kT_e = 33.07^{+16.81}_{-7.76}$  keV. From the analysis of the same observation, S. H. Ezhikode et al. (2020) reported  $E_{\text{cut}} = 132.75^{+98.32}_{-39.98}$  keV.

*SDSS J114921.52+532013.4*. This Seyfert 1 galaxy was observed once in 2016. From the Model 2a fit to the source spectrum, we found  $kT_e = 6.50^{+1.25}_{-0.97}$  keV.

## ORCID iDs

Indrani Pal  <https://orcid.org/0000-0002-7825-1526>  
 Claudio Ricci  <https://orcid.org/0000-0001-5231-2645>  
 S. Marchesi  <https://orcid.org/0000-0001-5544-0749>

## References

- Abramowicz, M. A., Czerny, B., Lasota, J. P., & Szuszkiewicz, E. 1988, *ApJ*, 332, 646  
 Akylas, A., & Georgantopoulos, I. 2021, *A&A*, 655, A60  
 Arnaud, K. A. 1996, in ASP Conf. Ser. 101, XSPEC: The First Ten Years, ed. G. H. Jacoby & J. Barnes (San Francisco, CA: ASP), 17

- Ballantyne, D. R., Bollenbacher, J. M., Brenneman, L. W., et al. 2014, *ApJ*, **794**, 62
- Baloković, M., Harrison, F. A., Madejski, G., et al. 2020, *ApJ*, **905**, 41
- Barua, S., Jithesh, V., Misra, R., et al. 2020, *MNRAS*, **492**, 3041
- Barua, S., Jithesh, V., Misra, R., et al. 2021, *ApJ*, **921**, 46
- Beloborodov, A. M. 1999, *ApJL*, **510**, L123
- Boissay, R., Ricci, C., & Paltani, S. 2016, *A&A*, **588**, A70
- Brandt, W. N., Mathur, S., & Elvis, M. 1997, *MNRAS*, **285**, L25
- Brightman, M., Masini, A., Ballantyne, D. R., et al. 2016, *ApJ*, **826**, 93
- Brightman, M., Silverman, J. D., Mainieri, V., et al. 2013, *MNRAS*, **433**, 2485
- Dadina, M. 2007, *A&A*, **461**, 1209
- Dadina, M. 2008, *A&A*, **485**, A17
- Denney, K. D., Watson, L. C., Peterson, B. M., et al. 2009, *ApJ*, **702**, 1353
- Diaz, Y., Hernández-García, L., Arévalo, P., et al. 2023, *A&A*, **669**, A114
- Elvis, M., Maccacaro, T., Wilson, A. S., et al. 1978, *MNRAS*, **183**, 129
- Ezhikode, S. H., Dewangan, G. C., Misra, R., & Philip, N. S. 2020, *MNRAS*, **495**, 3373
- Fabian, A. C., Lohfink, A., Kara, E., et al. 2015, *MNRAS*, **451**, 4375
- Feigelson, E. D., & Nelson, P. I. 1985, *ApJ*, **293**, 192
- García, J., & Kallman, T. R. 2010, *ApJ*, **718**, 695
- García, J., Kallman, T. R., & Mushotzky, R. F. 2011, *ApJ*, **731**, 131
- Guilbert, P. W., Fabian, A. C., & Rees, M. J. 1983, *MNRAS*, **205**, 593
- Haardt, F., & Maraschi, L. 1991, *ApJL*, **380**, L51
- Haardt, F., & Maraschi, L. 1993, *ApJ*, **413**, 507
- Harrison, F. A., Craig, W. W., Christensen, F. E., et al. 2013, *ApJ*, **770**, 103
- Hinkle, J. T., & Mushotzky, R. 2021, *MNRAS*, **506**, 4960
- Ho, L. C. 2008, *ARA&A*, **46**, 475
- Jin, C., Ward, M., & Done, C. 2012, *MNRAS*, **425**, 907
- Johnson, W. N., McNaron-Brown, K., Kurfess, J. D., et al. 1997, *ApJ*, **482**, 173
- Kamraj, N., Brightman, M., Harrison, F. A., et al. 2022, *ApJ*, **927**, 42
- Kamraj, N., Harrison, F. A., Baloković, M., Lohfink, A., & Brightman, M. 2018, *ApJ*, **866**, 124
- Kang, J., Wang, J., & Kang, W. 2020, *ApJ*, **901**, 111
- Kang, J.-L., & Wang, J.-X. 2022, *ApJ*, **929**, 141
- Kang, J.-L., Wang, J.-X., & Kang, W.-Y. 2021, *MNRAS*, **502**, 80
- Kara, E., García, J. A., Lohfink, A., et al. 2017, *MNRAS*, **468**, 3489
- Keek, L., & Ballantyne, D. R. 2016, *MNRAS*, **456**, 2722
- Liu, H., Luo, B., Brandt, W. N., et al. 2021, *ApJ*, **910**, 103
- Liu, T., Wang, J.-X., Yang, H., Zhu, F.-F., & Zhou, Y.-Y. 2014, *ApJ*, **783**, 106
- Lubiński, P., Beckmann, V., Gibaud, L., et al. 2016, *MNRAS*, **458**, 2454
- Lubiński, P., Zdziarski, A. A., Walter, R., et al. 2010, *MNRAS*, **408**, 1851
- Lynden-Bell, D. 1969, *Natur*, **223**, 690
- Malizia, A., Molina, M., Bassani, L., et al. 2014, *ApJL*, **782**, L25
- Malkan, M. A., & Sargent, W. L. W. 1982, *ApJ*, **254**, 22
- Malzac, J., Beloborodov, A. M., & Poutanen, J. 2001, *MNRAS*, **326**, 417
- Marchesi, S., Ajello, M., Marcotullini, L., et al. 2018, *ApJ*, **854**, 49
- Mattson, B. J., Weaver, K. A., & Reynolds, C. S. 2007, *ApJ*, **664**, 101
- McHardy, I. M., Gunn, K. F., Uttley, P., & Goad, M. R. 2005, *MNRAS*, **359**, 1469
- Mejía-Restrepo, J. E., Trakhtenbrot, B., Koss, M. J., et al. 2022, *ApJS*, **261**, 5
- Middei, R., Bianchi, S., Marinucci, A., et al. 2019, *A&A*, **630**, A131
- Molina, M., Bassani, L., Malizia, A., et al. 2009, *MNRAS*, **399**, 1293
- Molina, M., Bassani, L., Malizia, A., et al. 2013, *MNRAS*, **433**, 1687
- Molina, M., Malizia, A., Bassani, L., et al. 2019, *MNRAS*, **484**, 2735
- Moro, A. D., Alexander, D. M., Aird, J. A., et al. 2017, *ApJ*, **849**, 57
- Muchotrzeb, B., & Paczynski, B. 1982, *AcA*, **32**, 1
- Mushotzky, R. F., Done, C., & Pounds, K. A. 1993, *ARA&A*, **31**, 717
- Nicastro, F., Piro, L., De Rosa, A., et al. 2000, *ApJ*, **536**, 718
- Oh, K., Koss, M., Markwardt, C. B., et al. 2018, *ApJS*, **235**, 4
- Paczynski, B., & Bisnovaty-Kogan, G. 1981, *AcA*, **31**, 283
- Pal, I., & Stalin, C. S. 2023, *MNRAS*, **518**, 2529
- Pal, I., Stalin, C. S., Mallick, L., & Rani, P. 2022, *A&A*, **662**, A78
- Panagiotou, C., & Walter, R. 2019, *A&A*, **626**, A40
- Panagiotou, C., & Walter, R. 2020, *A&A*, **640**, A31
- Parker, M. L., Komossa, S., Kollatschny, W., et al. 2016, *MNRAS*, **461**, 1927
- Perola, G. C., Matt, G., Cappi, M., et al. 2002, *A&A*, **389**, 802
- Petrucci, P. O., Haardt, F., Maraschi, L., et al. 2001, *ApJ*, **556**, 716
- Porquet, D., Reeves, J. N., Grosso, N., Braitto, V., & Lobban, A. 2021, *A&A*, **654**, A89
- Rani, P., Stalin, C. S., & Goswami, K. D. 2019, *MNRAS*, **484**, 5113
- Ricci, C., Ho, L. C., Fabian, A. C., et al. 2018, *MNRAS*, **480**, 1819
- Ricci, C., & Trakhtenbrot, B. 2023, *NatAs*, **7**, 1282
- Ricci, C., Trakhtenbrot, B., Koss, M. J., et al. 2017, *ApJS*, **233**, 17
- Risaliti, G., Elvis, M., Fabbiano, G., Baldi, A., & Zezas, A. 2005, *ApJL*, **623**, L93
- Risaliti, G., Young, M., & Elvis, M. 2009, *ApJL*, **700**, L6
- Salpeter, E. E. 1964, *ApJ*, **140**, 796
- Serafinelli, R., Braitto, V., Reeves, J. N., et al. 2023, *A&A*, **672**, A10
- Shakura, N. I., & Sunyaev, R. A. 1973, *A&A*, **24**, 337
- Shemmer, O., Brandt, W. N., Netzer, H., Maiolino, R., & Kaspi, S. 2006, *ApJL*, **646**, L29
- Shemmer, O., Brandt, W. N., Netzer, H., Maiolino, R., & Kaspi, S. 2008, *ApJ*, **682**, 81
- Shields, G. A. 1978, *Natur*, **272**, 706
- Sun, W.-H., & Malkan, M. A. 1989, *ApJ*, **346**, 68
- Sunyaev, R. A., & Titarchuk, L. G. 1980, *A&A*, **86**, 121
- Tazaki, F., Ueda, Y., Terashima, Y., & Mushotzky, R. F. 2011, *ApJ*, **738**, 70
- Thorne, K. S. 1974, *ApJ*, **191**, 507
- Tortosa, A., Ricci, C., Ho, L. C., et al. 2023, *MNRAS*, **519**, 6267
- Tortosa, A., Ricci, C., Tombesi, F., et al. 2022, *MNRAS*, **509**, 3599
- Tortosa, A., Bianchi, S., Marinucci, A., Matt, G., & Petrucci, P. O. 2018, *A&A*, **614**, A37
- Trakhtenbrot, B., Ricci, C., Koss, M. J., et al. 2017, *MNRAS*, **470**, 800
- Turner, T. J., Reeves, J. N., Braitto, V., & Costa, M. 2018, *MNRAS*, **476**, 1258
- Ursini, F., Boissay, R., Petrucci, P.-O., et al. 2015, *A&A*, **577**, A38
- Ursini, F., Petrucci, P.-O., Matt, G., et al. 2016, *MNRAS*, **463**, 382
- Vasudevan, R. V., & Fabian, A. C. 2007, *MNRAS*, **381**, 1235
- Vasudevan, R. V., Mushotzky, R. F., & Gandhi, P. 2013, *ApJL*, **770**, L37
- Wang, J.-M., Du, P., Hu, C., et al. 2014, *ApJ*, **793**, 108
- Wang, J. M., & Netzer, H. 2003, *A&A*, **398**, 927
- Willingale, R., Starling, R. L. C., Beardmore, A. P., Tanvir, N. R., & O'Brien, P. T. 2013, *MNRAS*, **431**, 394
- Winkler, H. 1992, *MNRAS*, **257**, 677
- Zappacosta, L., Comastri, A., Civano, F., et al. 2018, *ApJ*, **854**, 33
- Zdziarski, A. A., Johnson, W. N., & Magdziarz, P. 1996, *MNRAS*, **283**, 193
- Zdziarski, A. A., Lubiński, P., Gilfanov, M., & Revnivtsev, M. 2003, *MNRAS*, **342**, 355
- Zdziarski, A. A., Lubiński, P., & Smith, D. A. 1999, *MNRAS*, **303**, L11
- Zdziarski, A. A., Poutanen, J., & Johnson, W. N. 2000, *ApJ*, **542**, 703
- Zhang, J.-X., Wang, J.-X., & Zhu, F.-F. 2018, *ApJ*, **863**, 71
- Zoghbi, A., Matt, G., Miller, J. M., et al. 2017, *ApJ*, **836**, 2
- Życki, P. T., Done, C., & Smith, D. A. 1999, *MNRAS*, **309**, 561